

THEME B

SIMULATION OF THE BEHAVIOR OF PROTOTYPES OF ROCKFILL DAMS DURING OVERTOPPING SCENARIOS. SEEPAGE EVOLUTION AND BEGINNING OF FAILURE

Joint theme between:



(International Center for Numerical Methods in Engineering)

Antonia Larese De Tetto Riccardo Rossi Eugenio Oñate



Polytechnic University of Madrid

Miguel Ángel Toledo Rafael Moran Hibber Campos,

CEDEX

Centre for Hydrographical Studies

Angel Lara M^a del Pilar Viña

Reference person:

Antonia Larese De Tetto (CIMNE)

antoldt@cimne.upc.edu

c/ Gran Capitán s/n

08034 Barcelona - Spain

Tel. +34 934 016 038 - Fax +34 934 016 517

TABLE OF CONTENTS

LIST OF TABLES	3
LIST OF FIGURES.....	4
INTRODUCTION.....	5
EXPERIMENTAL SETTINGS AND MEASUREMENTS.....	5
Instrumentation	5
Topographic analysis of slope failure.....	6
BENCHMARKS TESTS	8
CASE A) HOMOGENEOUS DAM	9
Geometry and material.....	9
A.1 No failure (seepage analysis)	11
A.2 Failure evolution.....	11
CASE B) CORE DAM.....	15
Geometry and material.....	15
B.1 No failure (seepage analysis)	17
B.2 Failure evolution.....	17
CASE C) IMPERMEABLE SCREEN DAM.....	21
Geometry and material.....	21
C.1 No failure (seepage analysis)	23
C.2 Failure evolution.....	23
ACKNOWLEDGEMENTS.....	25

LIST OF TABLES

Table 1. Summary of the upstream discharges for each considered case study.....	8
Table 2. Case A. Sensors distribution and position. The coordinates have to be intended referred to the reference system present in Figure 4.	11
Table 3. Case A.1. Bottom pressure heights at the steady state for an incoming discharge Q_{A1}	11
Table 4. Case A.2.1. Bottom pressure heights at the steady state for an incoming discharge Q_{A21} .	12
Table 5. Case A.2.2. Bottom pressure heights at the steady state for an incoming discharge Q_{A22} .	13
Table 6. Case A.2.3. Bottom pressure heights at the steady state for an incoming discharge Q_{A23} .	14
Table 7. Case B. Sensors distribution and position. The coordinates have to be intended referred to the reference system presented in Figure 9.....	16
Table 8. Case B.1. Bottom pressure heights at the steady state for an incoming discharge Q_{B1} .	17
Table 9. Case B.2.1. Bottom pressure heights at the steady state for an incoming discharge Q_{B21} .	18
Table 10. Case B.2.2. Bottom pressure heights at the steady state for an incoming discharge Q_{B22}	19
Table 11. Case B.2.3. Bottom pressure heights at the steady state for an incoming discharge Q_{B23} .	20
Table 12. Case C. Sensors distribution and coordinates with respect to the global reference system presented in Figure 13.	22
Table 13. Case C.1. Bottom pressure heights at the steady state for an incoming discharge Q_{C1} ...	23
Table 14. Case C.2.1. Bottom pressure heights at the steady state for an incoming discharge Q_{C21}	24
Table 15. Case C.2.1. Bottom pressure heights at the steady state for an incoming discharge Q_{C22}	24
Table 16 .Case C.2.3. Bottom pressure heights at the steady state for an incoming discharge Q_{C23}	25

LIST OF FIGURES

Figure 1. Pressure instrumentation.....	6
Figure 2. Length of failure. Characterization and operative measurement.....	6
Figure 3. Digital model of the slope to evaluate the advance degree of failure B.	7
Figure 4. Case A. Geometry of the experimental setting of the homogeneous dam and pressure sensor distribution.....	10
Figure 5. Case A. Some photos of the experimental channel and of and homogeneous dam.....	10
Figure 6. Case A.2.1. Digital model of the slope to evaluate the advance degree of failure B.....	12
Figure 7. Case A.2.2. Digital model of the slope to evaluate the advance degree of failure B.....	13
Figure 8. Case A.2.3. Digital model of the slope to evaluate the advance degree of failure B.....	14
Figure 9. Case B. Geometry of the experimental setting and of the dam and pressure sensor distribution. All the measurements are in millimetres.	16
Figure 10. Case B.2.1 Steady state stable configuration achieved for a discharge Q_{B21}	18
Figure 11. Case B.2.2 Steady state stable configuration achieved for a discharge Q_{B22}	19
Figure 12. Case B.2.3 Steady state stable configuration achieved for a discharge Q_{B23}	20
Figure 13. Case C. Geometry of the dam with impermeable screen in the upstream slope and position of the pressure sensors. All the dimensions have to be intended in cm.	22
Figure 14. Case C. Upper view of the dam.....	23

INTRODUCTION

In recent years the technology on embankments dams has developed sensibly due to the advances in soil mechanic, and in all related sciences. Nevertheless their vulnerability to overtopping still remains their weakest point in comparison with concrete structures.

The principal aim of this theme is the simulation of the initial stage of failure of the dam when an overtopping or an exceptional flood occurs.

A fluid-structure coupled problem has to be considered.

The sudden variation of the upstream conditions induces a quick evolution of a seepage line in the downstream shoulder. Non linear Darcy law has to be taken into account.

On the other hand the water, emerging from the toe of the dam, induces dragging of particles and possible mass sliding, depending on geometrical and material conditions.

UPM and CEDEX have carried out more than 70 experiments during the last two years. They analyzed the influence of a series of parameters on the failure mechanisms. These parameters are, for instance, the dimension of the rocks, the slope of the downstream part of the dam, the type of impermeable element used, and so on.

We propose to reproduce numerically three experiments analyzing the evolution of seepage and following initial stage of failure in the case of a homogeneous dam, of a dam with impermeable upstream face and of a dam with internal core. Experimental data, bottom pressure distribution and topographic analysis of the geometry of the dam during the failure can be compared with numerical results.

EXPERIMENTAL SETTINGS AND MEASUREMENTS

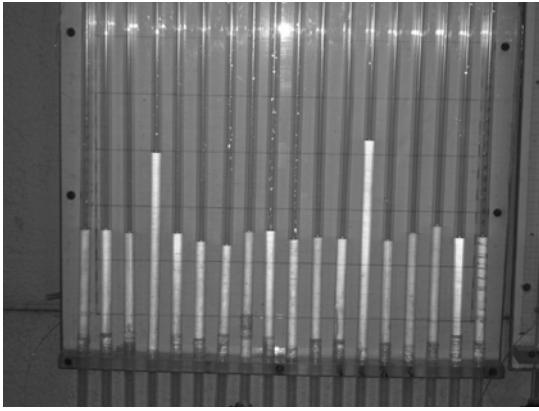
UPM and CEDEX have been developing more than 70 experiments in the last years to study deeply the phenomenon of overtopping in embankments dams focusing particularly on its initial phase, when the first breach appears in the downstream slope leading eventually to a complete failure.

For each experiment a sequence of incremental discharges is imposed. Every step (characterized by a value of incoming discharge) is analyzed when the stationary regime is reached. Bottom pressure distribution is measured. When partial failure of the downstream slope or movement of the same appears, a stabilization of the failure mechanism is achieved before calculating the bottom pressure distribution and the advance degree of failure with the help, in some cases, of a photogrammetric analysis of the new downstream slope stable configuration. The experiment ends when the failure of the dam is complete.

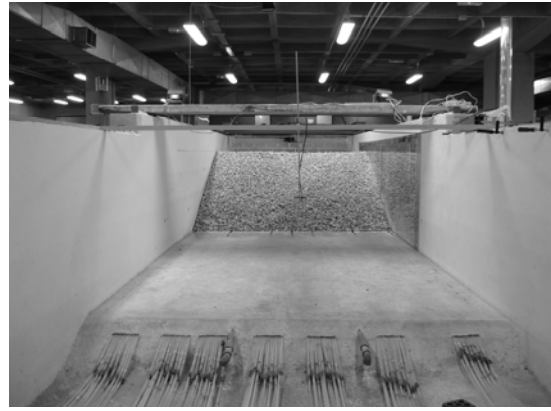
Instrumentation

Pressure sensors are inserted in the bottom of the experimental channels. In the case of the channel of case A and B, the UPM channel, the pressure sensors are 84. They are uniformly distributed in the bottom of the dam along 7 parallel lines as described in Case A and B sections. In the case of CEDEX channel (case C) the pressure sensors are 44. Their distribution will be detailed later on.

Pressure values at the stationary regime are read on millimetric panels (see Figure 1).



a) One of the panel for reading pressure heights.



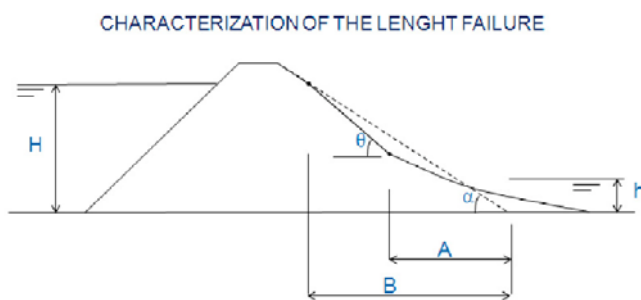
b) Front view of the channel with the pressure sensor tubes

Figure 1. Pressure instrumentation.

Topographic analysis of slope failure

The formation of the first breaches and their evolution are analyzed at each discharge step. When the stationary regime is achieved and the stable configuration of the slope is reached, the advance degree of failure (B in Figure 2a) is measured. It is by definition, the horizontal projection of the distance between the original downstream toe line and the higher point of the failed area. Colored strikes on the initial slope, help the measurement of B (see Figure 2b for an example).

In some of the experiments (case A for instance), a more detailed measurement of B is performed using a *close-object-photogrammetry-technique*. It consists on taking a series of photos in a very short time interval and continuing this sequence of photos till the end of the simulation. Through the re-elaboration of this data the creation of a digital model of the slope geometry evolution is possible and the dynamic failure is followed with high precision (see for instance Figure 3).



a) Schematic view of the length of failure B .



b) Visual measurement of the advance degree of failure with the help of coloured lines

Figure 2. Length of failure. Characterization and operative measurement.

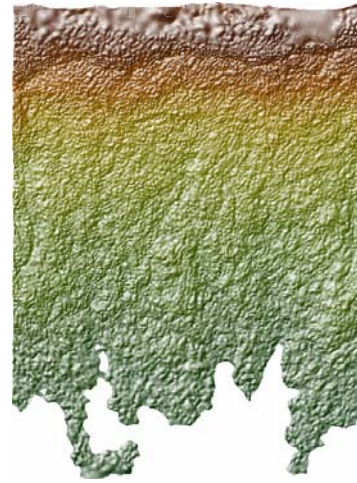
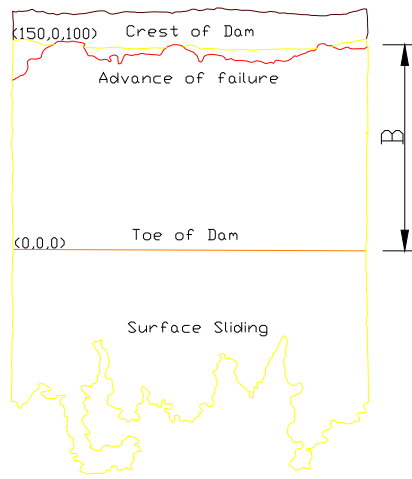


Figure 3. Digital model of the slope to evaluate the advance degree of failure B.

BENCHMARKS TESTS

The aim of this theme is the study of the structural response of a rockfill experimental dam for a given incoming/overtopping discharge.

Three different test-cases will be proposed:

- **Case A.** A homogeneous dam;
- **Case B.** A dam with internal core (simulation only of the downstream shoulder).
- **Case C.** A dam with upstream impermeable face;

For each case i ($i = A, B$ or C), two sub analyses are proposed:

- **Case i.1** Analysis of non linear seepage given an incoming/overtopping discharge.
Bottom pressure values at the stationary regime are provided.
- **Case i.2** Analysis of the evolution of failure given an incoming/overtopping discharge.
Bottom pressure values together with the measurements of the advance degree of failure at the stationary regime are provided for each experimental discharge.
Three different values of discharges are considered in this case.
Case i.2.j+1 has as initial configuration the final solution of **Case i.2.j** in terms of pressure and advance degree of failure.

Every sub case is characterized by a different upstream discharge. A summary of all the cases presented is given in Table 1.

	CASE A Homogeneous Dam	CASE B Core Dam	CASE C Dam with impermeable face
WITHOUT FAILURE Non linear seepage evolution analysis	A.1 Q=25.46l/s	B.1 Q=5.93l/s	C.1 Q=5.17l/s
WITH FAILURE Failure evolution analysis	A.2.1 Q=51.75l/s A.2.2 Q=69.07l/s A.2.3 Q=90.68l/s	B.2.1 Q=19.36l/s B.2.2 Q=30.45l/s B.2.3 Q=39.56l/s	C.2.1 Q=15.36l/s C.2.2 Q=25.05l/s C.2.3 Q=30.27l/s

Table 1. Summary of the upstream discharges for each considered case study.

CASE A) HOMOGENEOUS DAM

The first case study is a homogeneous dam. Although this kind of structure is radically different from a real dam, the study of the evolution of seepage and initial formation of breaching is very interesting. No overtopping can be reached in this case, the complete failure of the dam occurs before the overtopping discharge can be achieved. The experiment was performed by UPM.

Geometry and material

The granular material used in this experiment is homogeneous and has the following characteristics:

Porosity	= 0.4052;
Pore index	= 0.68;
Apparent specific weight	= 2.50 gr/cm ³
Dry density	= 1.49 gr/cm ³
Saturated density	= 1.91 gr/cm ³
D ₅₀	= 35.04mm.

The experimental setting is a channel of the UPM laboratories. The length of the channel is 13.535m, its width is 2.46m and its height is 1.31m. All details about the initial geometry of the channel and of the dam can be found in Figure 4.

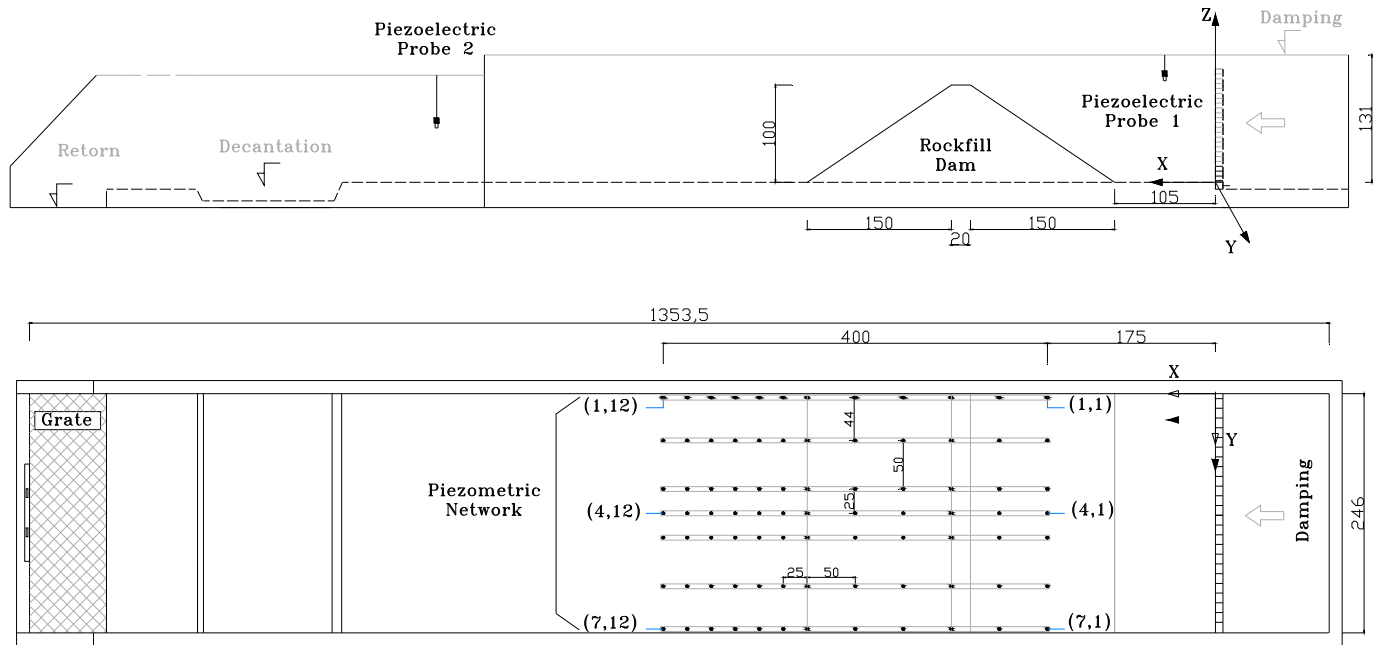


Figure 4. Case A. Geometry of the experimental setting of the homogeneous dam and pressure sensor distribution.



Figure 5. Case A. Some photos of the experimental channel and of and homogeneous dam

Pressure measurements are performed through a red of 36 sensors positioned at the bottom of the channel. They are distributed along three longitudinal lines. The detailed position of the sensors is reported in Table 2.

Sensor	X position (cm)	Y position (cm)	Sensor	X position (cm)	Y position (cm)	Sensor	X position (cm)	Y position (cm)
S (1,1)	175	4	S (4,1)	175	123	S (7,1)	175	242
S (1,2)	225	4	S (4,2)	225	123	S (7,2)	225	242
S (1,3)	275	4	S (4,3)	275	123	S (7,3)	275	242
S (1,4)	325	4	S (4,4)	325	123	S (7,4)	325	242
S (1,5)	375	4	S (4,5)	375	123	S (7,5)	375	242
S (1,6)	425	4	S (4,6)	425	123	S (7,6)	425	242
S (1,7)	450	4	S (4,7)	450	123	S (7,7)	450	242
S (1,8)	475	4	S (4,8)	475	123	S (7,8)	475	242
S (1,9)	500	4	S (4,9)	500	123	S (7,9)	500	242
S (1,10)	525	4	S (4,10)	525	123	S (7,10)	525	242
S (1,11)	550	4	S (4,11)	550	123	S (7,11)	550	242
S (1,12)	575	4	S (4,12)	575	123	S (7,12)	575	242

Table 2. Case A. Sensors distribution and position. The coordinates have to be intended referred to the reference system present in Figure 4.

A.1 No failure (seepage analysis)

No relevant movements in the down stream slope are registered for an incoming discharge of

$$Q_{A1} = 25.46\text{l/s.}$$

Therefore the problem of evolution of the seepage line can be analyzed considering the dam as fixed.

The bottom pressure distribution is presented in Table 3.

Sensor	Pressure (cm)	Sensor	Pressure (cm)	Sensor	Pressure (cm)
S (1,1)	-	S (4,1)	-	S (7,1)	-
S (1,2)	-	S (4,2)	-	S (7,2)	-
S (1,3)	27.7	S (4,3)	28.0	S (7,3)	28.0
S (1,4)	24.1	S (4,4)	24.1	S (7,4)	24.0
S (1,5)	18.7	S (4,5)	18.9	S (7,5)	18.6
S (1,6)	5.0	S (4,6)	4.5	S (7,6)	3.7
S (1,7)	-	S (4,7)	-	S (7,7)	-
S (1,8)	-	S (4,8)	-	S (7,8)	-
S (1,9)	-	S (4,9)	-	S (7,9)	-
S (1,10)	-	S (4,10)	-	S (7,10)	-
S (1,11)	-	S (4,11)	-	S (7,11)	-
S (1,12)	-	S (4,12)	-	S (7,12)	-

Table 3. Case A.1. Bottom pressure heights at the steady state for an incoming discharge Q_{A1} .

A.2 Failure evolution

Increasing the incoming discharges the downstream slope starts to deform and a coupled problem should be considered.

Three sub cases are proposed and data of the stationary state of each one are provided.

A.2.1

Imposing an incoming discharge of

$$Q_{A21} = 51.75\text{l/s}$$

the downstream material starts to move and part of the toe of the dam starts to slip.

At the steady state the pressure distribution registered is the one presented in Table 4.

Sensor	Pressure (cm)	Sensor	Pressure (cm)	Sensor	Pressure (cm)
S (1,1)	-	S (4,1)	-	S (7,1)	-
S (1,2)	-	S (4,2)	-	S (7,2)	-
S (1,3)	43.1	S (4,3)	43.1	S (7,3)	43.5
S (1,4)	36.2	S (4,4)	36.1	S (7,4)	36.0
S (1,5)	24.2	S (4,5)	24.9	S (7,5)	24.7
S (1,6)	10.2	S (4,6)	9.1	S (7,6)	9.6
S (1,7)	-	S (4,7)	-	S (7,7)	-
S (1,8)	-	S (4,8)	-	S (7,8)	-
S (1,9)	-	S (4,9)	-	S (7,9)	-
S (1,10)	-	S (4,10)	-	S (7,10)	-
S (1,11)	-	S (4,11)	-	S (7,11)	-
S (1,12)	-	S (4,12)	-	S (7,12)	-

Table 4. Case A.2.1. Bottom pressure heights at the steady state for an incoming discharge Q_{A21} .

The advance degree of failure is

$$B = 71\text{cm};$$

It is deduced from the digital model of the deformed slope shown in Figure 6.

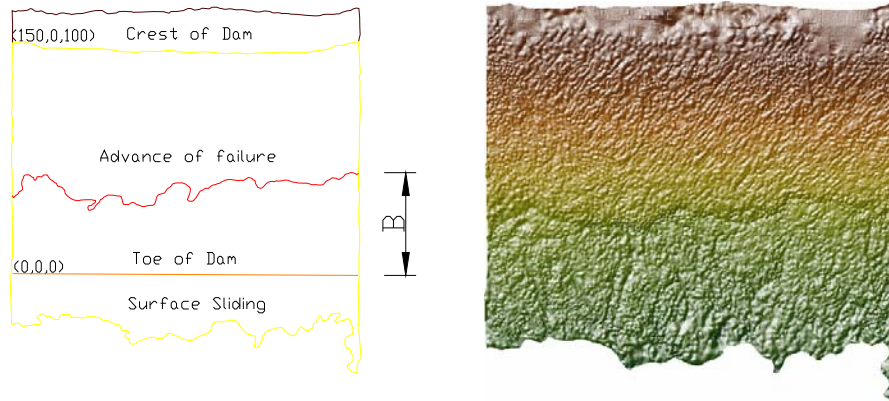


Figure 6. Case A.2.1. Digital model of the slope to evaluate the advance degree of failure B.

A.2.2

In the case of an incoming discharge

$$Q_{A22} = 69.07\text{l/s}$$

the correspondent pressure distribution is given in Table 5.

Sensor	Pressure (cm)	Sensor	Pressure (cm)	Sensor	Pressure (cm)
S (1,1)	-	S (4,1)	-	S (7,1)	-
S (1,2)	-	S (4,2)	-	S (7,2)	-
S (1,3)	51.0	S (4,3)	51.0	S (7,3)	51.3
S (1,4)	41.5	S (4,4)	41.5	S (7,4)	41.4
S (1,5)	27.4	S (4,5)	28.1	S (7,5)	27.6
S (1,6)	13.0	S (4,6)	13.1	S (7,6)	13.6
S (1,7)	-	S (4,7)	-	S (7,7)	-
S (1,8)	-	S (4,8)	-	S (7,8)	-
S (1,9)	-	S (4,9)	-	S (7,9)	-
S (1,10)	-	S (4,10)	-	S (7,10)	-
S (1,11)	-	S (4,11)	-	S (7,11)	-
S (1,12)	-	S (4,12)	-	S (7,12)	-

Table 5. Case A.2.2. Bottom pressure heights at the steady state for an incoming discharge Q_{A22} .

The advance degree of failure for the present case is

$$B = 107.8\text{cm};$$

and the digital model of the deformed slope is given in Figure 7.

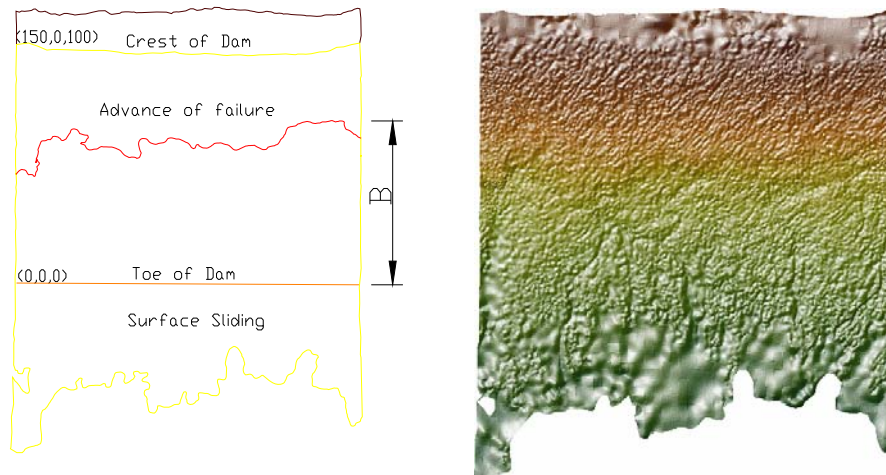


Figure 7. Case A.2.2. Digital model of the slope to evaluate the advance degree of failure B.

A.2.3

In the case of an incoming discharge

$$Q_{A23} = 90.681/\text{s}$$

the correspondent pressure distribution is given in Table 6.

Sensor	Pressure (cm)	Sensor	Pressure (cm)	Sensor	Pressure (cm)
S (1,1)	-	S (4,1)	-	S (7,1)	-
S (1,2)	-	S (4,2)	-	S (7,2)	-
S (1,3)	57.3	S (4,3)	57.4	S (7,3)	57.4
S (1,4)	45.2	S (4,4)	44.5	S (7,4)	44.8
S (1,5)	25.9	S (4,5)	26.1	S (7,5)	24.8
S (1,6)	19.6	S (4,6)	18.4	S (7,6)	20
S (1,7)	-	S (4,7)	-	S (7,7)	-
S (1,8)	-	S (4,8)	-	S (7,8)	-
S (1,9)	-	S (4,9)	-	S (7,9)	-
S (1,10)	-	S (4,10)	-	S (7,10)	-
S (1,11)	-	S (4,11)	-	S (7,11)	-
S (1,12)	-	S (4,12)	-	S (7,12)	-

Table 6. Case A.2.3. Bottom pressure heights at the steady state for an incoming discharge Q_{A23} .

The advance degree of failure for the present case is

$$B = 155.6\text{cm};$$

It is taken from the digital model of the downstream slope presented in Figure 8.

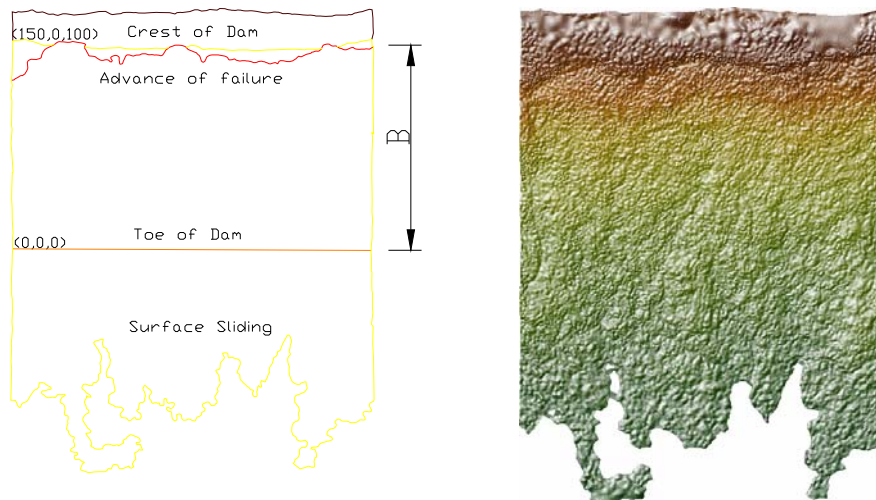


Figure 8. Case A.2.3. Digital model of the slope to evaluate the advance degree of failure B.

CASE B) CORE DAM

The second experiment that we propose is a core dam. In this particular case the core is considered rigid and its possible failure is not taken into account. The experiment was performed by UPM.

Geometry and material

The material used in this case is the same than in case A.

Porosity	= 0.4052;
Pore index	= 0.68;
Apparent specific weight	= 2.50 gr/cm ³
Dry density	= 1.49 gr/cm ³
Saturated density	= 1.91 gr/cm ³
D ₅₀	= 35.04mm.

Where porosity is by definition the volume of empty space over the total volume and D₅₀ is the mean diameter.

The geometrical setting of this experiment is described in Figure 9, where also the sensor distribution is given, nevertheless their coordinates are detailed also in Table 7.

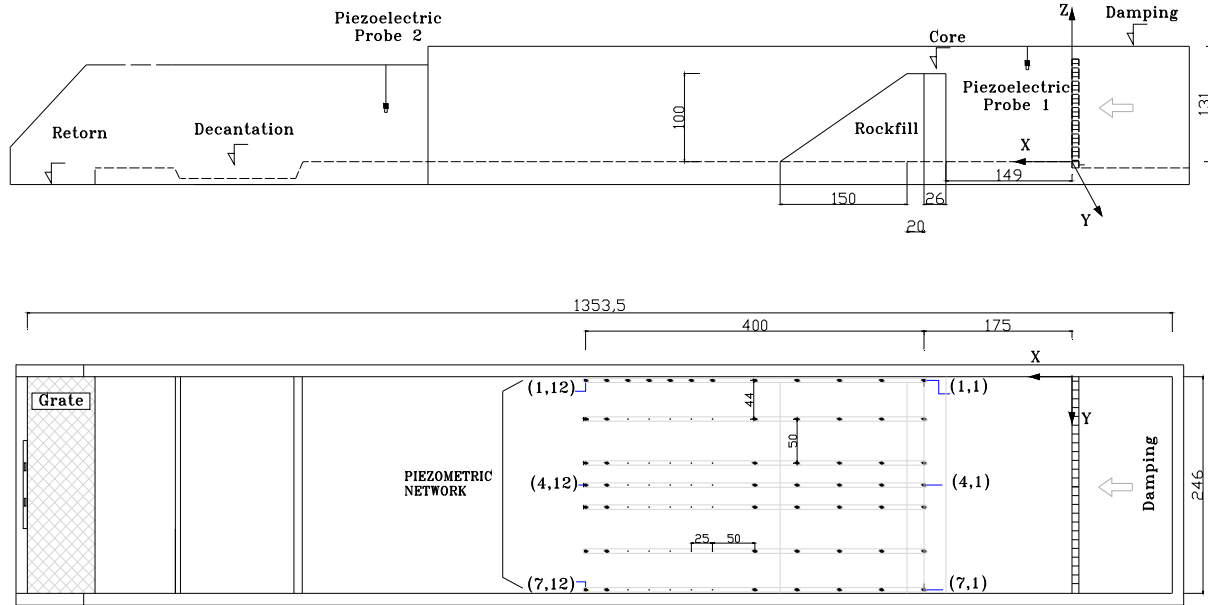


Figure 9. Case B. Geometry of the experimental setting and of the dam and pressure sensor distribution. All the measurements are in millimetres.

The experimental channel is the same than in Case A. The core dam is simulated reproducing only the downstream shoulder.

Sensor	X (cm)	Y (cm)
S (1,1)	175	4
S (1,2)	225	4
S (1,3)	275	4
S (1,4)	325	4
S (1,5)	375	4
S (1,6)	425	4
S (1,7)	450	4
S (1,8)	475	4
S (1,9)	500	4
S (1,10)	525	4
S (1,11)	550	4
S (1,12)	575	4

Sensor	X (cm)	Y (cm)
S (2,1)	175	48
S (2,2)	225	48
S (2,3)	275	48
S (2,4)	325	48
S (2,5)	375	48
S (2,6)	425	48
S (2,7)	450	48
S (2,8)	475	48
S (2,9)	500	48
S (2,10)	525	48
S (2,11)	550	48
S (2,12)	575	48

Sensor	X (cm)	Y (cm)
S (3,1)	175	98
S (3,2)	225	98
S (3,3)	275	98
S (3,4)	325	98
S (3,5)	375	98
S (3,6)	425	98
S (3,7)	450	98
S (3,8)	475	98
S (3,9)	500	98
S (3,10)	525	98
S (3,11)	550	98
S (3,12)	575	98

Sensor	X (cm)	Y (cm)
S (4,1)	175	123
S (4,2)	225	123
S (4,3)	275	123
S (4,4)	325	123
S (4,5)	375	123
S (4,6)	425	123
S (4,7)	450	123
S (4,8)	475	123
S (4,9)	500	123
S (4,10)	525	123
S (4,11)	550	123
S (4,12)	575	123

Sensor	X (cm)	Y (cm)
S (5,1)	175	148
S (5,2)	225	148
S (5,3)	275	148
S (5,4)	325	148
S (5,5)	375	148
S (5,6)	425	148
S (5,7)	450	148
S (5,8)	475	148
S (5,9)	500	148
S (5,10)	525	148
S (5,11)	550	148
S (5,12)	575	148

Sensor	X (cm)	Y (cm)
S (6,1)	175	198
S (6,2)	225	198
S (6,3)	275	198
S (6,4)	325	198
S (6,5)	375	198
S (6,6)	425	198
S (6,7)	450	198
S (6,8)	475	198
S (6,9)	500	198
S (6,10)	525	198
S (6,11)	550	198
S (6,12)	575	198

Sensor	X (cm)	Y (cm)
S (7,1)	175	242
S (7,2)	225	242
S (7,3)	275	242
S (7,4)	325	242
S (7,5)	375	242
S (7,6)	425	242
S (7,7)	450	242
S (7,8)	475	242
S (7,9)	500	242
S (7,10)	525	242
S (7,11)	550	242
S (7,12)	575	242

Table 7. Case B. Sensors distribution and position. The coordinates have to be intended referred to the reference system presented in Figure 9.

B.1 No failure (seepage analysis)

No relevant movements in the downstream slope are registered for an incoming discharge of

$$Q_{B1} = 5.931/s.$$

Therefore the problem of evolution of the seepage line can be analyzed considering the dam as fixed.

The bottom pressure distribution is presented in Table 8.

Sensor	Pres (cm)
S (1,1)	15.6
S (1,2)	14.0
S (1,3)	11.2
S (1,4)	3.2
S (1,5)	2.4
S (1,6)	2.4
S (1,7)	2.4
S (1,8)	2.4
S (1,9)	2.4
S (1,10)	2.4
S (1,11)	2.4
S (1,12)	2.4

Sensor	Pres (cm)
S (2,1)	15.6
S (2,2)	14
S (2,3)	11.2
S (2,4)	2.5
S (2,5)	2.4
S (2,6)	2.4
S (2,7)	2.4
S (2,8)	2.4
S (2,9)	2.4
S (2,10)	2.4
S (2,11)	2.4
S (2,12)	2.4

Sensor	Pres (cm)
S (3,1)	15.6
S (3,2)	14.0
S (3,3)	11.2
S (3,4)	2.9
S (3,5)	2.4
S (3,6)	2.4
S (3,7)	2.4
S (3,8)	2.4
S (3,9)	2.4
S (3,10)	2.4
S (3,11)	2.4
S (3,12)	2.4

Sensor	Pres (cm)
S (4,1)	15.6
S (4,2)	14.0
S (4,3)	11.2
S (4,4)	3.5
S (4,5)	2.4
S (4,6)	2.4
S (4,7)	2.4
S (4,8)	2.4
S (4,9)	2.4
S (4,10)	2.4
S (4,11)	2.4
S (4,12)	2.4

Sensor	Pres (cm)
S (5,1)	15.6
S (5,2)	14.0
S (5,3)	11.2
S (5,4)	2.9
S (5,5)	2.4
S (5,6)	2.4
S (5,7)	2.4
S (5,8)	2.4
S (5,9)	2.4
S (5,10)	2.4
S (5,11)	2.4
S (5,12)	2.4

Sensor	Pres (cm)
S (6,1)	15.6
S (6,2)	13.7
S (6,3)	11.2
S (6,4)	2.9
S (6,5)	2.4
S (6,6)	2.4
S (6,7)	2.4
S (6,8)	2.4
S (6,9)	2.4
S (6,10)	2.4
S (6,11)	2.4
S (6,12)	2.4

Sensor	Pres (cm)
S (7,1)	15.4
S (7,2)	13.5
S (7,3)	11.0
S (7,4)	2.7
S (7,5)	2.4
S (7,6)	2.4
S (7,7)	2.4
S (7,8)	2.4
S (7,9)	2.4
S (7,10)	2.4
S (7,11)	2.4
S (7,12)	2.4

Table 8. Case B.1. Bottom pressure heights at the steady state for an incoming discharge Q_{B1} .

B.2 Failure evolution

B.2.1

The second step of discharge is

$$Q_{B21} = 19.361/s$$

In this case the downstream slope starts to deform. Once a stable configuration is achieved, the pressure distribution is read and registered. It is detailed in Table 9.

Sensor	Pres (cm)
S (1,1)	33.6
S (1,2)	28.7
S (1,3)	21.4
S (1,4)	6.8
S (1,5)	4.0
S (1,6)	4.0
S (1,7)	4.0
S (1,8)	4.0
S (1,9)	4.0
S (1,10)	4.0
S (1,11)	4.0
S (1,12)	4.0

Sensor	Pres (cm)
S (2,1)	33.6
S (2,2)	28.7
S (2,3)	22.1
S (2,4)	7.0
S (2,5)	4.0
S (2,6)	4.0
S (2,7)	4.0
S (2,8)	4.0
S (2,9)	4.0
S (2,10)	4.0
S (2,11)	4.0
S (2,12)	4.0

Sensor	Pres (cm)
S (3,1)	33.6
S (3,2)	28.6
S (3,3)	22.1
S (3,4)	7.0
S (3,5)	4.0
S (3,6)	4.0
S (3,7)	4.0
S (3,8)	4.0
S (3,9)	4.0
S (3,10)	4.0
S (3,11)	4.0
S (3,12)	4.0

Sensor	Pres (cm)
S (4,1)	33.6
S (4,2)	28.6
S (4,3)	21.9
S (4,4)	6.8
S (4,5)	4.0
S (4,6)	4.0
S (4,7)	4.0
S (4,8)	4.0
S (4,9)	4.0
S (4,10)	4.0
S (4,11)	4.0
S (4,12)	4.0

Sensor	Pres (cm)
S (5,1)	33.3
S (5,2)	28.6
S (5,3)	21.5
S (5,4)	6.6
S (5,5)	4.0
S (5,6)	4.0
S (5,7)	4.0
S (5,8)	4.0
S (5,9)	4.0
S (5,10)	4.0
S (5,11)	4.0
S (5,12)	4.0

Sensor	Pres (cm)
S (6,1)	33.5
S (6,2)	28.4
S (6,3)	21.7
S (6,4)	6.5
S (6,5)	4.0
S (6,6)	4.0
S (6,7)	4.0
S (6,8)	4.0
S (6,9)	4.0
S (6,10)	4.0
S (6,11)	4.0
S (6,12)	4.0

Sensor	Pres (cm)
S (7,1)	33.1
S (7,2)	28.4
S (7,3)	21.2
S (7,4)	6.5
S (7,5)	4.0
S (7,6)	4.0
S (7,7)	4.0
S (7,8)	4.0
S (7,9)	4.0
S (7,10)	4.0
S (7,11)	4.0
S (7,12)	4.0

Table 9. Case B.2.1. Bottom pressure heights at the steady state for an incoming discharge Q_{B21} .



Figure 10. Case B.2.1 Steady state stable configuration achieved for a discharge Q_{B21} .

The advance degree of failure is measured visually. It is

$$B = 32 \text{ cm};$$

The stable deformed configuration of the downstream slope is shown in Figure 10.

B.2.2

In the case of an incoming discharge

$$Q_{B22} = 30.451/\text{s}$$

the pressure distribution at the stable configuration is given in Table 10.

Sensor	Pres (cm)
S (1,1)	41.6
S (1,2)	36.5
S (1,3)	25.0
S (1,4)	11.1
S (1,5)	4.8
S (1,6)	4.8
S (1,7)	4.8
S (1,8)	4.8
S (1,9)	4.8
S (1,10)	4.8
S (1,11)	4.8
S (1,12)	4.8

Sensor	Pres (cm)
S (2,1)	41.6
S (2,2)	36.5
S (2,3)	26.2
S (2,4)	10.3
S (2,5)	4.8
S (2,6)	4.8
S (2,7)	4.8
S (2,8)	4.8
S (2,9)	4.8
S (2,10)	4.8
S (2,11)	4.8
S (2,12)	4.8

Sensor	Pres (cm)
S (3,1)	41.7
S (3,2)	36.4
S (3,3)	26.1
S (3,4)	10.4
S (3,5)	4.8
S (3,6)	4.8
S (3,7)	4.8
S (3,8)	4.8
S (3,9)	4.8
S (3,10)	4.8
S (3,11)	4.8
S (3,12)	4.8

Sensor	Pres (cm)
S (4,1)	41.8
S (4,2)	36.5
S (4,3)	25.6
S (4,4)	10.4
S (4,5)	4.8
S (4,6)	4.8
S (4,7)	4.8
S (4,8)	4.8
S (4,9)	4.8
S (4,10)	4.8
S (4,11)	4.8
S (4,12)	4.8

Sensor	Pres (cm)
S (5,1)	41.4
S (5,2)	36.5
S (5,3)	25.1
S (5,4)	10.7
S (5,5)	4.8
S (5,6)	4.8
S (5,7)	4.8
S (5,8)	4.8
S (5,9)	4.8
S (5,10)	4.8
S (5,11)	4.8
S (5,12)	4.8

Sensor	Pres (cm)
S (6,1)	41.9
S (6,2)	36
S (6,3)	25.8
S (6,4)	9.8
S (6,5)	4.8
S (6,6)	4.8
S (6,7)	4.8
S (6,8)	4.8
S (6,9)	4.8
S (6,10)	4.8
S (6,11)	4.8
S (6,12)	4.8

Sensor	Pres (cm)
S (7,1)	41.5
S (7,2)	36.3
S (7,3)	25.3
S (7,4)	10.5
S (7,5)	4.8
S (7,6)	4.8
S (7,7)	4.8
S (7,8)	4.8
S (7,9)	4.8
S (7,10)	4.8
S (7,11)	4.8
S (7,12)	4.8

Table 10. Case B.2.2. Bottom pressure heights at the steady state for an incoming discharge Q_{B22} .



Figure 11. Case B.2.2 Steady state stable configuration achieved for a discharge Q_{B22} .

The advance degree of failure is measured visually. It is

$$B = 68\text{cm};$$

The stable deformed configuration of the downstream slope is shown in Figure 11.

B.2.3

In the case of an incoming discharge

$$Q_{B23} = 39.56 \text{ l/s}$$

the correspondent pressure distribution is given in Table 11.

Sensor	Pres (cm)						
S (1,1)	46.9	S (2,1)	46.7	S (3,1)	46.7	S (4,1)	46.9
S (1,2)	41.7	S (2,2)	41.6	S (3,2)	41.5	S (4,2)	41.5
S (1,3)	27.7	S (2,3)	29.1	S (3,3)	29.1	S (4,3)	28.9
S (1,4)	15.6	S (2,4)	14.4	S (3,4)	16.5	S (4,4)	17
S (1,5)	5.3	S (2,5)	5.3	S (3,5)	5.3	S (4,5)	5.3
S (1,6)	5.3	S (2,6)	5.3	S (3,6)	5.3	S (4,6)	5.3
S (1,7)	5.3	S (2,7)	5.3	S (3,7)	5.3	S (4,7)	5.3
S (1,8)	5.3	S (2,8)	5.3	S (3,8)	5.3	S (4,8)	5.3
S (1,9)	5.3	S (2,9)	5.3	S (3,9)	5.3	S (4,9)	5.3
S (1,10)	5.3	S (2,10)	5.3	S (3,10)	5.3	S (4,10)	5.3
S (1,11)	5.3	S (2,11)	5.3	S (3,11)	5.3	S (4,11)	5.3
S (1,12)	5.3	S (2,12)	5.3	S (3,12)	5.3	S (4,12)	5.3

Sensor	Pres (cm)	Sensor	Pres (cm)	Sensor	Pres (cm)
S (5,1)	46.3	S (6,1)	46.6	S (7,1)	46.4
S (5,2)	41.5	S (6,2)	40.7	S (7,2)	41.1
S (5,3)	28.2	S (6,3)	28.5	S (7,3)	27.4
S (5,4)	16.6	S (6,4)	15	S (7,4)	16.2
S (5,5)	5.3	S (6,5)	5.3	S (7,5)	5.3
S (5,6)	5.3	S (6,6)	5.3	S (7,6)	5.3
S (5,7)	5.3	S (6,7)	5.3	S (7,7)	5.3
S (5,8)	5.3	S (6,8)	5.3	S (7,8)	5.3
S (5,9)	5.3	S (6,9)	5.3	S (7,9)	5.3
S (5,10)	5.3	S (6,10)	5.3	S (7,10)	5.3
S (5,11)	5.3	S (6,11)	5.3	S (7,11)	5.3
S (5,12)	5.3	S (6,12)	5.3	S (7,12)	5.3

Table 11. Case B.2.3. Bottom pressure heights at the steady state for an incoming discharge Q_{B23} .



Figure 12. Case B.2.3 Steady state stable configuration achieved for a discharge Q_{B23} .

The advance degree of failure is measured visually. It is

$$B = 140.5 \text{ cm};$$

The stable deformed configuration of the downstream slope is shown in Figure 12.

CASE C) IMPERMEABLE SCREEN DAM

The third and last case proposed is a dam with an impermeable upstream screen. This is experimentally simulated by a plastic fill that fully covers the upstream slope and it is glued to the side wall of the experimental channel. This experiment has been carried out by CEDEX.

Geometry and material

The geometry of the experimental setting is presented in Figure 13. The homogeneous material used in this case has the following characteristics:

Porosity	= 0.4052;
Pore index	= 0.68;
Apparent specific weight	= 2.50 gr/cm ³
Dry density	= 1.49 gr/cm ³
Saturated density	= 1.91 gr/cm ³
D ₅₀	= 35.04mm.

The experimental setting and the sensor distribution is presented in Figure 13. The coordinates of these latter can be found in Table 12.

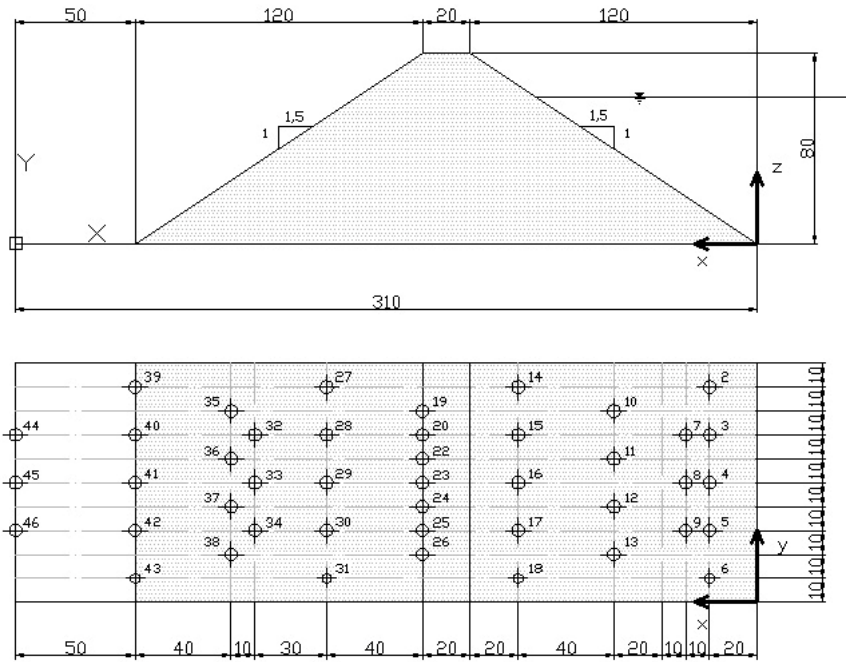


Figure 13. Case C. Geometry of the dam with impermeable screen in the upstream slope and position of the pressure sensors. All the dimensions have to be intended in cm.

Sensor	X position	Y position	Sensor	X position	Y position	Sensor	X position	Y position
2	20	90	11	60	60	20	140	70
3	20	70	12	60	40	22	140	60
4	20	50	13	60	20	23	140	50
5	20	30	14	100	90	24	140	40
6	20	10	15	100	70	25	140	30
7	30	70	16	100	50	26	140	20
8	30	50	17	100	30	27	180	90
9	30	30	18	100	10	28	180	70
10	60	80	19	140	80	29	180	50
30	180	30	39	260	90			
31	180	10	40	260	70			
32	210	70	41	260	50			
33	210	50	42	260	30			
34	210	30	43	260	10			
35	220	80	44	310	70			
36	220	60	45	310	50			
37	220	40	46	310	30			
38	220	20						

Table 12. Case C. Sensors distribution and coordinates with respect to the global reference system presented in Figure 13.

C.1 No failure (seepage analysis)



Figure 14. Case C. Upper view of the dam.

$$Q_{C21} = 5.171/s$$

Sensor	Pressure	Sensor	Pressure	Sensor	Pressure
2	20.26cm	11	17.98cm	20	15.50cm
3	19.11cm	12	19.06cm	22	18.09cm
4	19.22cm	13	18.93cm	23	18.64cm
5	18.53cm	14	18.27cm	24	19.08cm
6	19.20cm	15	19.20cm	25	17.87cm
7	19.08cm	16	18.27cm	26	18.02cm
8	22.07cm	17	18.60cm	27	15.86cm
9	17.85cm	18	18.69cm	28	15.81cm
10	19.06cm	19	19.24cm	29	14.24cm

Sensor	Pressure	Sensor	Pressure
30	13.64cm	39	5.75cm
31	14.93cm	40	4.71cm
32	11.41cm	41	4.20cm
33	11.56cm	42	5.31cm
34	18.80cm	43	3.45cm
35	10.99cm	44	3.82cm
36	10.15cm	45	3.87cm
37	11.01cm	46	5.35cm
38	11.28cm		

Table 13. Case C.1. Bottom pressure heights at the steady state for an incoming discharge Q_{C1} .

C.2 Failure evolution

C.2.1

The second step of discharge is

$$Q_{C21} = 15.361/s$$

In this case the downstream slope starts to deform. Once a stable configuration is achieved, the pressure distribution is read and registered. It is detailed in Table 14.

Sensor	Pressure	Sensor	Pressure	Sensor	Pressure
2	38.44 cm	11	37.25 cm	20	35.50 cm
3	36.39 cm	12	37.54 cm	22	35.50 cm
4	38.20 cm	13	37.16 cm	23	36.39 cm
5	37.27 cm	14	37.07 cm	24	36.08 cm
6	37.27 cm	15	37.14 cm	25	35.24 cm
7	36.81 cm	16	37.05 cm	26	35.48 cm
8	37.58 cm	17	36.92 cm	27	29.53 cm
9	37.25 cm	18	37.69 cm	28	29.55 cm
10	37.45 cm	19	36.28 cm	29	28.23 cm

Sensor	Pressure	Sensor	Pressure
30	28.74 cm	39	6.09 cm
31	28.58 cm	40	6.51 cm
32	22.50 cm	41	5.49 cm
33	23.52 cm	42	6.62 cm
34	26.26 cm	43	5.98 cm
35	21.64 cm	44	6.05 cm
36	19.73 cm	45	6.00 cm
37	20.46 cm	46	5.67 cm
38	20.46 cm		

Table 14. Case C.2.1. Bottom pressure heights at the steady state for an incoming discharge Q_{C21} .

The advance degree of failure is measured with visual technique. It is

$$B_{C21} = 24\text{cm};$$

C.2.2

In the case of an incoming discharge

$$Q_{C22} = 25.05\text{l/s}$$

the correspondent pressure distribution is given in Table 15.

Sensor	Pressure	Sensor	Pressure	Sensor	Pressure
2	49.78 cm	11	48.77 cm	20	45.30 cm
3	49.23 cm	12	48.94 cm	22	45.81 cm
4	49.89 cm	13	48.88 cm	23	46.85 cm
5	48.90 cm	14	49.01 cm	24	46.67 cm
6	48.90 cm	15	49.12 cm	25	45.41 cm
7	48.97 cm	16	48.41 cm	26	44.68 cm
8	48.88 cm	17	48.28 cm	27	37.21 cm
9	48.75 cm	18	49.25 cm	28	36.66 cm
10	49.03 cm	19	47.44 cm	29	36.75 cm

Sensor	Pressure	Sensor	Pressure
30	36.57 cm	39	9.28 cm
31	37.25 cm	40	10.14 cm
32	25.85 cm	41	9.81 cm
33	26.56 cm	42	10.52 cm
34	30.21 cm	43	10.25 cm
35	20.53 cm	44	7.49 cm
36	21.34 cm	45	7.62 cm
37	23.05 cm	46	7.60 cm
38	21.10 cm		

Table 15. Case C.2.1. Bottom pressure heights at the steady state for an incoming discharge Q_{C22} .

The advance degree of failure is measured with visual technique. It is

$$B_{C22} = 59.00\text{cm};$$

C.2.3

In the case of an incoming discharge

$$Q_{C23} = 30.27\text{l/s}$$

the correspondent pressure distribution is given in Table 16.

Sensor	Pressure	Sensor	Pressure	Sensor	Pressure
2	53.30 cm	11	52.60 cm	20	48.62 cm
3	52.73 cm	12	52.71 cm	22	48.77 cm
4	53.37 cm	13	52.40 cm	23	49.92 cm
5	52.42 cm	14	52.77 cm	24	50.14 cm
6	52.35 cm	15	53.33 cm	25	48.79 cm
7	52.66 cm	16	52.11 cm	26	48.44 cm
8	53.75 cm	17	51.91 cm	27	39.35 cm
9	52.58 cm	18	53.33 cm	28	30.82 cm
10	53.11 cm	19	50.94 cm	29	38.80 cm

Sensor	Pressure	Sensor	Pressure
30	39.22 cm	39	14.14 cm
31	39.62 cm	40	15.05 cm
32	29.00 cm	41	14.05 cm
33	29.95 cm	42	15.80 cm
34	32.98 cm	43	14.94 cm
35	24.36 cm	44	8.72 cm
36	25.17 cm	45	8.74 cm
37	27.45 cm	46	8.59 cm
38	25.77 cm		

Table 16 .Case C.2.3. Bottom pressure heights at the steady state for an incoming discharge Q_{C23}

The advance degree of failure is measured with visual technique. It is

$$B_{C23} = 114.00\text{cm}.$$

ACKNOWLEDGEMENTS

The research was supported by the E-DAM project of the National Plan R+D of the Spanish Ministry of Science and Innovation I+D BIA2010-21350-C03-00.

XI ICOLD BENCHMARK WORKSHOP ON NUMERICAL ANALYSIS OF DAMS

Valencia, October 20-21, 2011

SOLUTION OF THEME B

**COUPLING EULERIAN AND LAGRANGIAN MODELS TO SIMULATE SEEPAGE AND EVOLUTION
OF FAILURE IN PROTOTYPE ROCKFILL DAMS**

Larese, Antonia¹

Rossi, Riccardo²

Oñate, Eugenio³

CONTACT

Antonia Larese, Centre Internacional de Mètodes Numèrics en Enginyeria (CIMNE), c/ Gran Capitán s/n, 08034 Barcelona Spain. E-mail: antoldt@cimne.upc.edu Tel. +34 93 401 60 38.

Summary

This work presents a model which allows considering the interaction between rockfill dams and the water.

The fluid behaviour is analyzed on an Eulerian fixed mesh. A level set technique is employed to track the evolution of the free surface. An edge based approach is used to solve efficiently the modified form of the Navier-Stokes equations.

The dam response is evaluated on a Lagrangian moving mesh using PFEM. A visco-rigid constitutive model is used to describe the structural behaviour and collapse of rockfill under fluid dynamic forces.

Mohr-Coulomb is the failure criteria adopted in the calculation.

Finally a nodal projection algorithm allows the transferring of information through non matching meshes.

¹ Centre Internacional de Mètodes Numèrics en Enginyeria (CIMNE), Barcelona, Spain.
UPC, BarcelonaTech, Campus Norte UPC, 08034 Barcelona, Spain

² Centre Internacional de Mètodes Numèrics en Enginyeria (CIMNE), Barcelona, Spain.
UPC, BarcelonaTech, Campus Norte UPC, 08034 Barcelona, Spain.

³ Centre Internacional de Mètodes Numèrics en Enginyeria (CIMNE), Barcelona, Spain.
UPC, BarcelonaTech, Campus Norte UPC, 08034 Barcelona, Spain.

1. Introduction

The principal aim of this work is the development of a tool for the simulation of the initial stage of failure of a rockfill dam when an overtopping or an exceptional flood occur.

According to the new regulations many dams and dikes exhibit a potential to experience overtopping during high flood events. Climate change induced by global warming is, for instance, one of the main causes that might lead to more devastating flooding than ever. In the case of a dam failure, loss of life and economic damage are the direct cost of such event. Their magnitude is strictly dependent on the water depth and velocity but also on the warning time, and on the presence of population. Therefore the possibility of predicting the effect of an exceptional flooding is a crucial point to reduce its devastating consequences. Unfortunately this is currently limited by the lack of a precise knowledge of the phenomenon and by the absence of a suitable computational method which can simulate the sudden dynamic change in seepage and flow conditions and predict accurately the subsequent onset and evolution of breaching.

XPRES (XPRES [13]) and E-DAMS (E-DAMS [1]) projects have been thought exactly to make a step ahead in the study of overspilling of rockfill dams and the initial phase of failure.

On the one hand the Polytechnic University of Madrid (UPM), the Centre for Hydrographical Studies of CEDEX have been in charged of the experimental analysis, whereas the Centre Internacional de Mètodes Numèrics en Enginyeria (CIMNE) has been developing an innovative computational approach to the phenomenon whose preliminary results are shown in this work.

The numerical method used in the code is briefly introduced in the next section. The fluid model performances are then tested in the solution of A1, B1, and C1 cases of Theme B of the XI Benchmark Workshop on Numerical Analysis of Dams. Whereas the coupled code is used for the solution of A2, B2, and C2 cases.

1. Description of the code

The code used in the simulations is being developed in CIMNE by the authors and it is a module of KRATOS multiphysics, an open source C++ framework for building multi-disciplinary finite element programs (Kratos [4], Dadvand et al. [2]).

It is based on combination of Eulerian level set techniques and Lagrangian Particle Finite Element Method (PFEM [10]). This is done in order to optimize the coupling between the dynamic effect of water inside and outside the dam, with the structural deformation and collapse induced on the down stream shoulder.

Both the water and the dam are studied using a continuum mechanics approach. Therefore a single element does not coincide with a granular particle but rather represents a cluster of them.

The variables of the problem are: the Darcy velocity, water pressure as well as the velocity and pressure of the dam, considered as a continuum.

In the fluid model, the classical form of the governing equations for an incompressible fluid are here modified, inserting the effect of porosity and the non linear relation given by the Ergun's modification to Darcy's law (Zienkiewicz et al.[15]). The governing equations obtained reduce to the classical form of the Navier-Stokes equations if the porous medium is no longer present allowing the simultaneous treatment of the water behavior both outside and inside the dam. The dam is studied using a visco-rigid model. The breaching formation and the consequent beginning of granular flow are analyzed with particular interest. The characterization of the failure process is dealt with by combining new numerical models with experimental tests on physical models of different sizes and scales.

1.1. Fluid module

Classical studies of fluid flow into porous media can't be used for the analysis of the water motion within the rockfill of a dam. Traditionally water is considered in slow motion or as a stationary load (Zienkiewicz et al.[14]). On the contrary in the case of an overtopping, the possibility to follow the rapid transition of the water level in the downstream slope is a key point for the identification of the beginning of the failure mechanism.

In flux through rockfill, the local fluid velocities have been observed not to be linearly related to the pressure drop. In fact it was experimentally proved that over certain average dimension of the particles, Darcy law is not anymore valid. In the present model a quadratic Darcy law is thus chosen using Ergun coefficients.

A crucial feature of the method is that both the seepage flow inside the dam and the water outside of it are considered in a single formulation, which greatly simplifies dealing with the complete simulation of the problem. In this sense the Navier-Stokes equations are modified so to take into account the presence of the porous medium. Note that the fully dynamic case is considered, including the convection effects.

The problem to solve is

$$\begin{aligned} \rho_f \partial_t \mathbf{u} + \rho_f \bar{\mathbf{u}} \cdot \nabla \mathbf{u} + n \nabla p_f - 2 \nabla \cdot \mu \nabla^s \mathbf{u} - n \rho_f \mathbf{g} + \mathbf{D} &= \mathbf{0} \\ \nabla \cdot \mathbf{u} &= 0 \end{aligned} \quad (1)$$

where \mathbf{u} is the fluid Darcy velocity, $\bar{\mathbf{u}}$ is the fluid velocity, p the fluid pressure, μ and ρ_f the water dynamic viscosity and density respectively, n the porosity and \mathbf{g} the gravity force vector. \mathbf{D} is the Darcy term which, following Ergun theory, takes the form

$$\mathbf{D} = \frac{\mu}{k} \mathbf{u} + \frac{1.75}{\sqrt{150}} \frac{\rho}{\sqrt{k}} \frac{|\mathbf{u}|}{n^{3/2}} \mathbf{u}. \quad (2)$$

Where k is the permeability of the medium.

The fluid solver uses an edge-based approach which leads to a very efficient semi-explicit algorithm (Rossi et al. [12], Larese [6]). Its particular structure allows an easy parallelization which dramatically improves the efficiency of the model.

The motion of the fluid is described using an Eulerian framework.

A level set approach is used to represent the free surface.

1.2. Structure module

The structural behavior of the dam is heavily influenced by its interaction with the flow of water, to the point that an embankment dam is typically considered as failed at the very moment at which the water arrives to overspill the dam crest, thus inducing a massive erosion of the downstream side.

Recent experimental campaigns show however evidence that such assumption is over-conservative as the dam still has some resistance to offer even in condition of overspill. The practical finding is that the failure mode is incremental rather than brittle so that the dam deforms but does not fail at once, even during overspill events.

The objective of the numerical model is thus to offer a prediction on the safety of dams during critical hydrological events.

Under the assumption that the rockfill size is small with respect to the overall size of the structure, a continuous description is used for the dam body.

Since typically very little is known about the geotechnical characterization of the rockfill, the numerical model for the dam body assumes a visco-rigid constitutive behavior. No elasticity is present.

The dam is calculated as a non-Newtonian material in which stiffness is regulated by the value of viscosity. This means that it is completely rigid until reaching the yield stress (τ_0). Therefore when this value is exceeded, the viscosity dramatically decreases and the material starts flowing. The viscosity will recover its initial value when the shear stresses do not overcome the yield threshold any more.

The problem to solve is then

$$\begin{aligned} \rho_s \partial_t \mathbf{u}_s + \rho_s \mathbf{u}_s \cdot \nabla^s \mathbf{u}_s + \nabla p'_s - 2 \nabla \cdot \tilde{\mu}_s \nabla \mathbf{u}_s - \rho_s \mathbf{g} + (1 - n) \nabla p_f - \mathbf{D} &= \mathbf{0} \\ \nabla \cdot \mathbf{u}_s &= 0 \end{aligned} \quad (3)$$

Where \mathbf{u}_s and p'_s are the dam velocity and effective pressure, ρ_s is the dry density and $\tilde{\mu}_s$ is the non-Newtonian variable viscosity. Its variability is defined using a regularized law defined by Papanastasiou (Papanastasiou [9]).

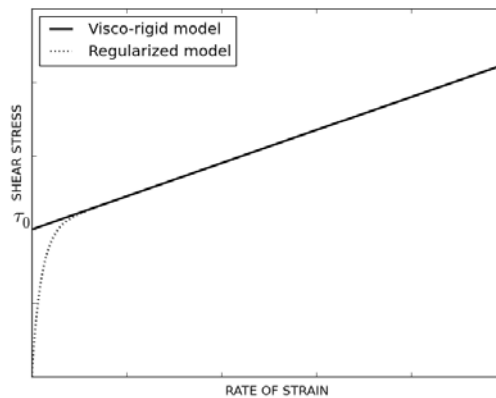


Figure 1. Comparison between the bilinear visco-rigid model and its regularized version proposed by Papanastasiou (Papanastasiou [9]). The closeness between the two curves is regulated by a smoothing parameter.

In Figure 1 the visco rigid model and its regularization are compared.

Finally in order to simulate a granular material (not a Bingham plastics) the yield stress is evaluated following a Mohr-Coulomb failure criterion without cohesion.

The problem is non linear both from the material and the geometrical point of view. Large displacements and strains are implicitly taken into account simulating the rockfill as a high viscosity granular “fluid”.

Since the structural domain is expected to undergo severe deformation as the failure progresses, the kinematic model has to adapt dynamically to such deformations. The use of the Particle Finite Element Method provides the necessary flexibility with a remeshing mechanism (Larese et al. [5], Oñate et al.[7]). It has already been successfully used in a wide range of problems (Oñate et al. [8], Ryzhakov et al. [11])

A stabilized equal-order velocity-pressure element technology is chosen so to guarantee a locking free behavior. The method is fully implicit.

1.3. Coupling procedure

The use of two different solution methods for the dam and the fluid leads implicitly to a staggered scheme.

The coupling is done through the Darcy term \mathbf{D} of equation 2 and the gradient of fluid pressure which are evaluated in the fluid field and projected on the dam mesh. On the other hand the dam configuration (i.e. the porosity distribution in space), is evaluated in the PFEM model and projected then to the Eulerian mesh in order to define the new boundary conditions for the fluid problem.

The flow chart of the entire simulation process can be schematically summarized by the following steps:

1. SOLVE the water free surface flow and seepage problem calculating VELOCITY and PRESSURE field in an EULERIAN fixed mesh;
2. PROJECT the water PRESSURE GRADIENT on the dam;
3. PROJECT the non linear DARCY TERM on the dam;
4. CALCULATE the structural response in terms of STRESS and STRAIN in a Lagrangian mesh, using PFEM;
5. PROJECT the new configuration of the dam in terms of POROSITY distribution on the Eulerian fluid domain;
6. PROJECT the DAM VELOCITY on the Eulerian fluid domain (to evaluate the Darcy term);
7. Go back to step 1.

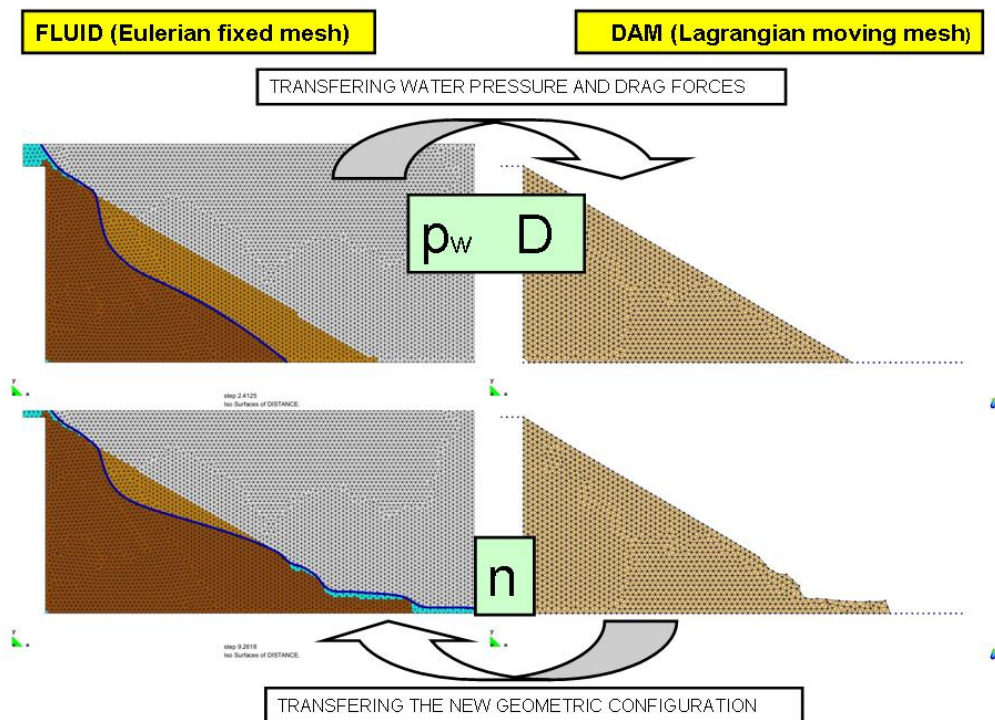


Figure 2. Summary of the basic steps of the global numerical algorithm.

2. Case study

In the following sections the simulation of the experimental tests of theme B of the XI Benchmark Workshop on Numerical Analysis of dams, are reported and commented. For geometrical data and experimental results, the consultation of theme B is recommended. Cases A1, B1, and C1 are calculated using only the fluid code whereas the remaining cases are evaluated using the coupled one.

2.1. Case A1

The fluid code is used to evaluate the pressure head distribution at the stationary regime.

The code was conceived to analyze the transitory phase of the discharge, allowing inserting flood hydrograms as input although in these examples this capability is not required.

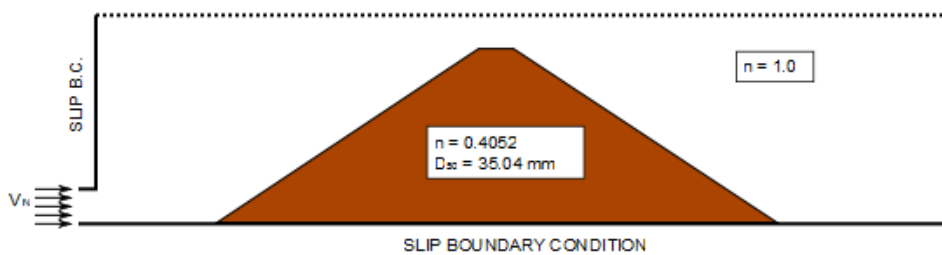


Figure 3. Case A1. Qualitative model geometry and boundary conditions.

A control domain is defined. The dam is described imposing the experimental value of porosity n and average diameter D_{50} . The inlet of water is set in the lower left part of the domain. Water progressively fills the domain till reaching the stationary regime. Figure 3 shows a qualitative model with the boundary conditions. The mesh is fixed and it is composed by 16.000 linear triangular elements like shown in Figure 4.

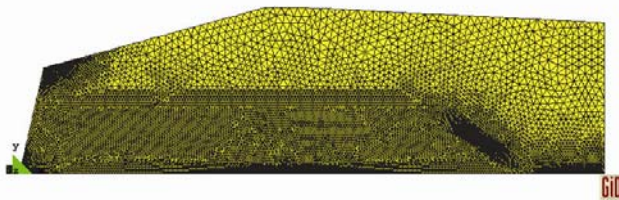


Figure 4. Case A1. 2d mesh. 16.000 linear triangular elements



Figure 5. Case A1. 3d mesh. 1.260.000 linear tetrahedral elements.

Figure 6 shows a perfect matching between experimental and numerical pressure heads at the stationary regime. The numerical output are compared with the line of sensors situated at $Y = 1.23\text{m}$.

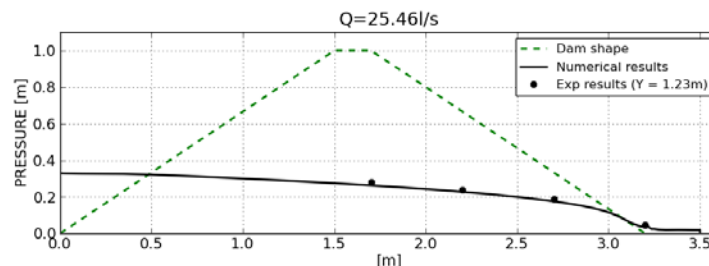


Figure 6. Case A1. 2d comparison between experimental and numerical pressure heads at stationary

regime.

The analyzed seepage problem is naturally 2d due to the regularity in plant of the channels. Nevertheless results for case A1 are also obtained in a 3d model composed by 1.300.000 linear tetrahedral (Figure 5) and are shown in Figure 7-a,b,c.

The water level in the 3d model is a bit lower than in the 2d case due to the larger mesh considered (this can affect the level set procedure to track the evolution of the free surface) and to the possible presence of a small mass loss (additional considerations on this problem can be found in Larese [6]).

Finally 2 and 3d output are compared also at transitory regime in Figure 8.

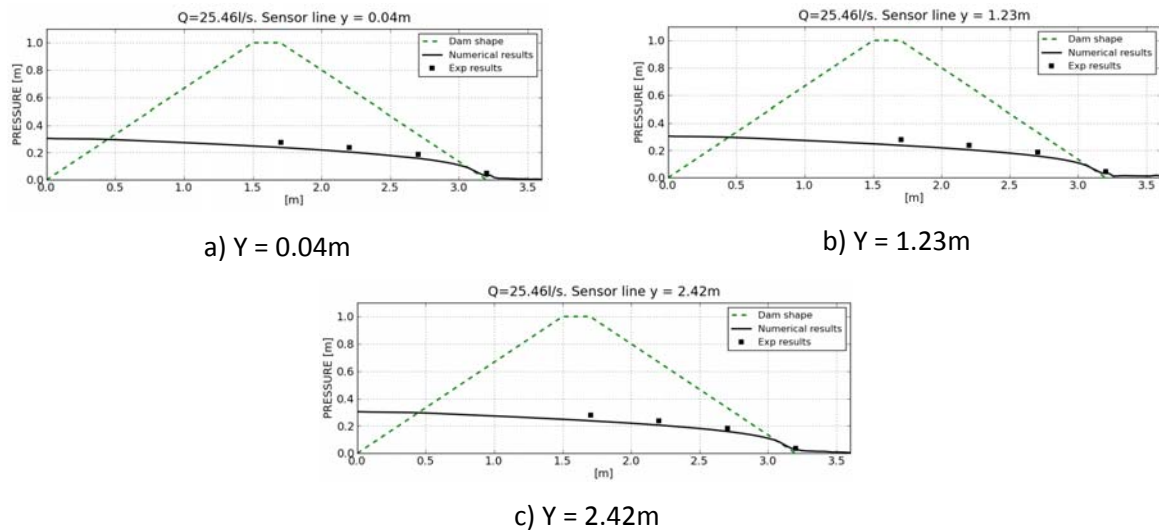


Figure 7. Case A1. 3d comparison between experimental and numerical results along the three sensors lines indicated in theme B.

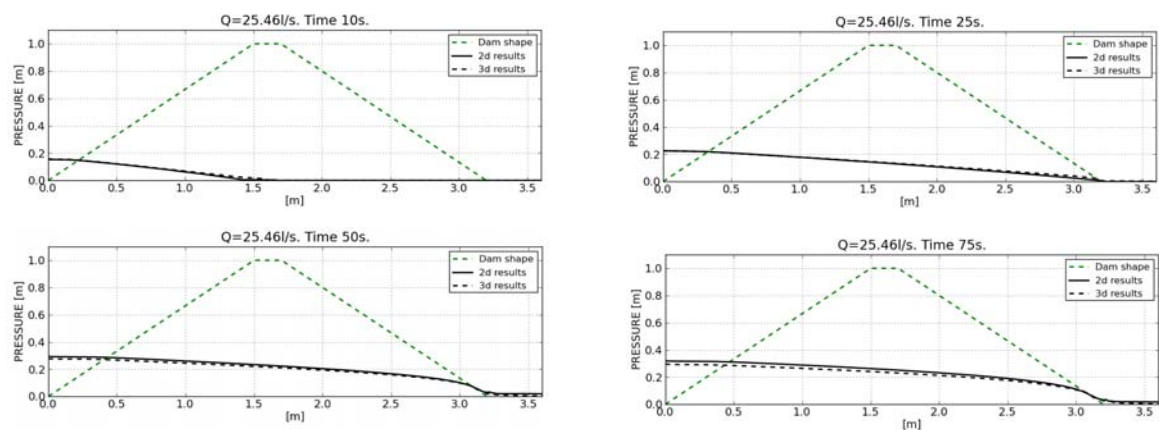


Figure 8. Case A1. Comparison between 3d and 2d numerical results in the transitory regime at 10s, 25s, 50s, 75s.

2.2. Case A2

In cases A21, A22 and A23, the models are exactly the same in term of geometry, meshing, initial and boundary conditions, except for the incoming discharge. The fluid model is constructed with the same criteria used in case A1 with the only difference that no granular material is present like can be

appreciated in the upper part of Figure 9. The porosity distribution and its characteristics are passed to the fluid model by the dam structural model at each time step.

The dam model is constructed in a Lagrangian framework. This implies modeling only the material domain (i.e. the dam initial shape and the walls if present). The necessary input parameters to define the properties of the rockfill are: porosity, D_{50} , dry density (taken from the theme B) and internal friction angle.

The friction angle is the only unavailable experimental data. It is fixed at 40° for A cases. Porosity and permeability are considered fixed in time according to experimental observation.

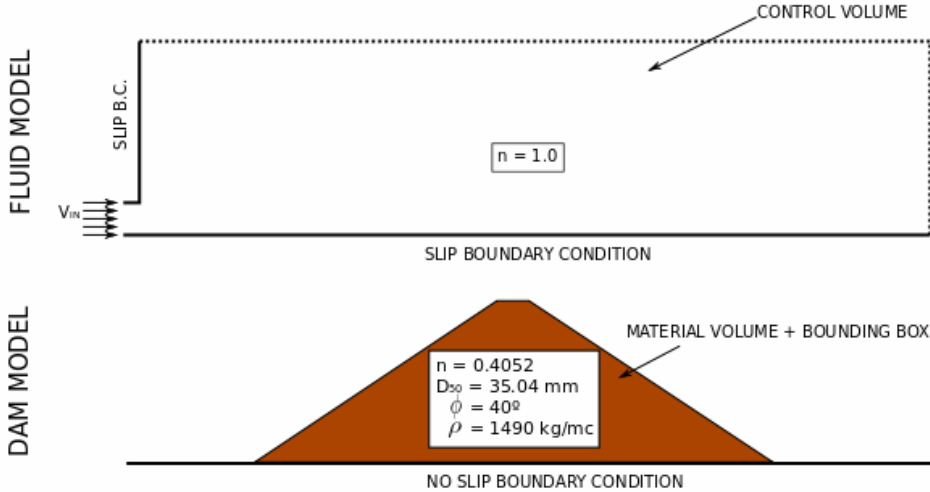


Figure 9. Cases A2. Fluid and dam qualitative models and boundary conditions for the coupled analysis.

The mesh used in the calculation is shown in Figure 10 and it is composed of 3.400 linear triangular elements.

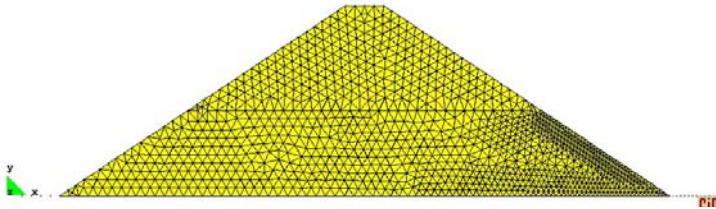


Figure 10. Cases A2. 2d mesh of the dam model. 3.400 linear triangular elements.

In the following three sections the numerical results are compared with the experimental data of cases A21, A22 and A23.

A preliminary remark on the interpretation of the experimental data should be made here. The experimental B length of failure is by definition the horizontal projection of the position of the higher particles that moves. This movement is not quantified. In the present work it was conventionally chosen to consider that an element moves if its total displacement is higher than the average dimension of the granular material (0.03m). This choice can be discussed and, as it will be shown later on, it does often make our model too much deformable. Nevertheless this empirical criterion was used in all the models in order to allow a comparison.

In the following sections the comparison between the experimental data and the numerical results is shown in terms of length of failure for case A21, A22, A23 respectively. The pressure head distribution at the stationary regime for each case is presented as well.

2.2.1. Case A21: $Q=51.75\text{/s}$

A very good accordance can be seen between experimental and numerical length of failure and the model evaluate correctly the head of pressure at the out come of the dam where the estimation is more important (see Figure 11).

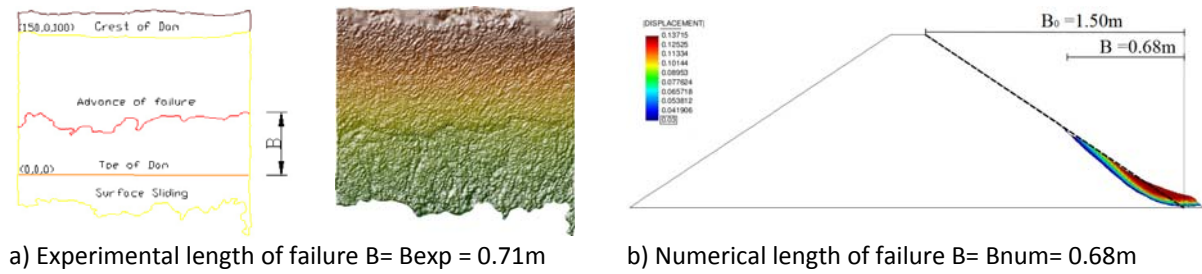


Figure 11. Case A21. 2d comparison between experimental and numerical length of failure.

Looking at the pressure head distribution (Figure 12), although a good accordance is obtained at the toe of the dam, the experimental free surface seems to have a higher slope than the numerical one. This can be the signal of an internal variation of the material conditions (such as porosity, permeability) that is not taken into account in the model.

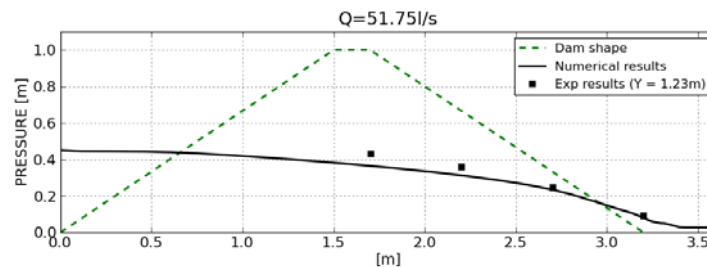
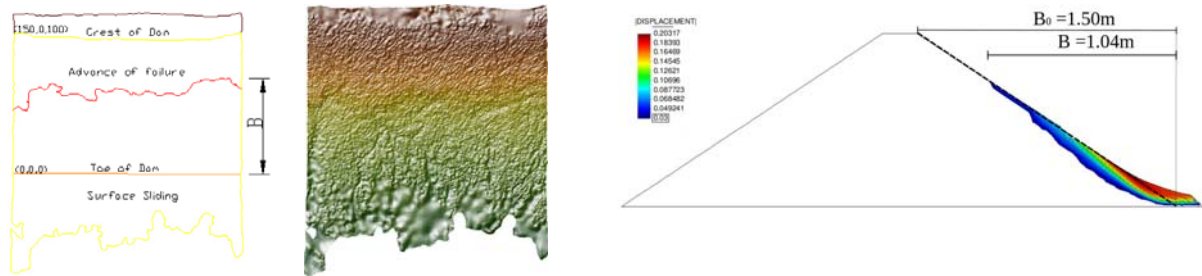


Figure 12. Case A21. 2d comparison between experimental and numerical pressure heads at stationary regime.

2.2.2. Case A22: $Q=69.07\text{/s}$

As well as in case A21 a good evaluation of the length of failure in case A22 can be observed in Figure 13 and the pressure head (Figure 14) gives satisfactory results. Nevertheless the same considerations done in case A21 can be applied here.



a) Experimental length of failure $B = B_{exp} = 1.08\text{m}$ b) Numerical length of failure $B = B_{num} = 1.04\text{ m}$

Figure 13. Case A22. 2d comparison between experimental and numerical length of failure.

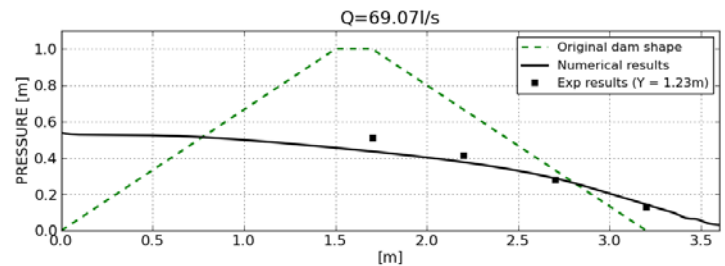
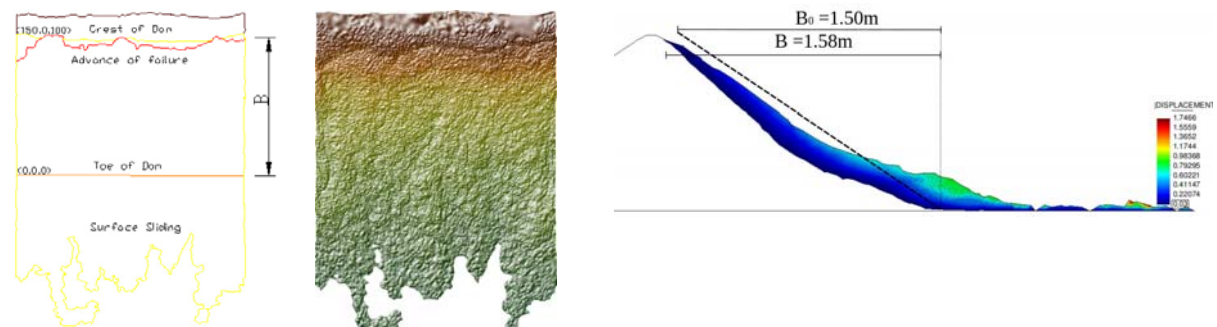


Figure 14. Case A22. 2d comparison between experimental and numerical pressure heads at stationary regime.

2.2.3. Case A23: $Q=90.68\text{ l/s}$

The failure in case A23 achieved the crest of the dam as expected according to the experiment. This can be appreciated in Figure 15.



a) Experimental length of failure $B = B_{exp} = 1.56\text{m}$ b) Numerical length of failure $B = B_{num} = 1.58\text{ m}$

Figure 15. Case A23. 2d comparison between experimental and numerical length of failure.

In this model the pressure head presents a lower experimental value where the water exits from the dam. The contraction of the flux can be induced by the absence of the rockfill that flowed away during the failure mechanism. This leads to the conclusion that the failed material in the numerical model is more rigid than in the real case. Its accumulation over the original toe of the dam induces a higher value of pressure than in the experiment.

On the other hand also in this case the free surface presents a smoother profile in the numerical results (see Figure 16).

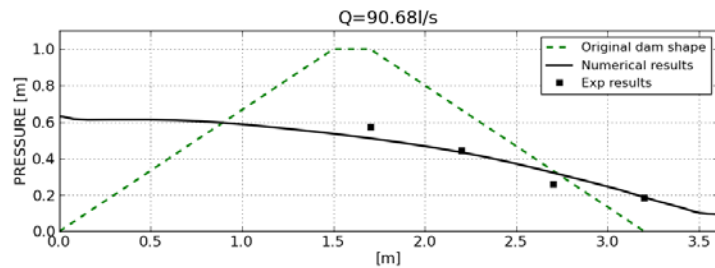


Figure 16. Case A23. 2d comparison between experimental and numerical pressure heads at stationary regime.

2.3. Case B1

When studying the behavior of a dam with internal core, according to experiments, only the downstream toe is modeled.

The water entrance is put in the upper left part omitting the simulation of the filling of the reservoir that is useless in the present analysis.

The model is constructed in the same way than case A1 explained in section 2.1. See Figure 17 for a qualitative model and boundary conditions and to see the mesh used for the calculation.

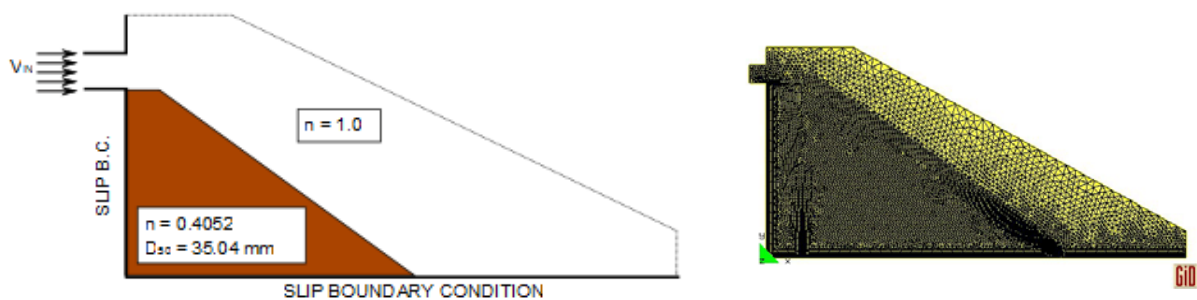


Figure 17. Case B1. Qualitative model geometry and boundary conditions on the left. Calculation mesh on the right (16.200 linear triangular elements).

Case B and C present an additional difficulty in the fluid dynamic problem. In fact it is particularly challenging to correctly simulate the falling jet of water (especially if the income water velocity is very slow), without suffering serious mass loss. The good accordance between experimental and numerical pressure heads confirms that this problem is not affecting significantly these models.

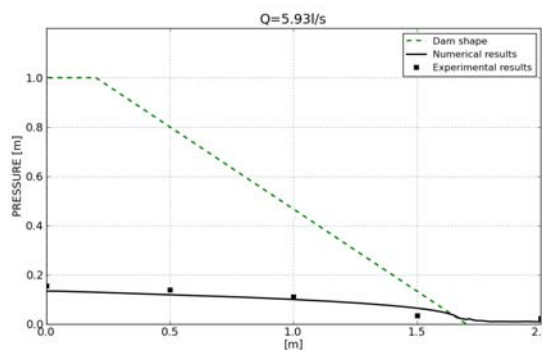


Figure 18. Case B1. 2d comparison between experimental and numerical pressure heads at stationary regime.

In Figure 18 the comparison between numerical and experimental results is shown. The lower value of experimental pressure head at the toe of the dam seems to indicate a small sliding of particle (not considered in the B1 model) although experimentalists indicates that no failure is present with the discharge of case B1.

2.4. Case B2

The construction of the model is similar to what already explained in section 2.2 for the A2 cases and it is shown in Figure 19.

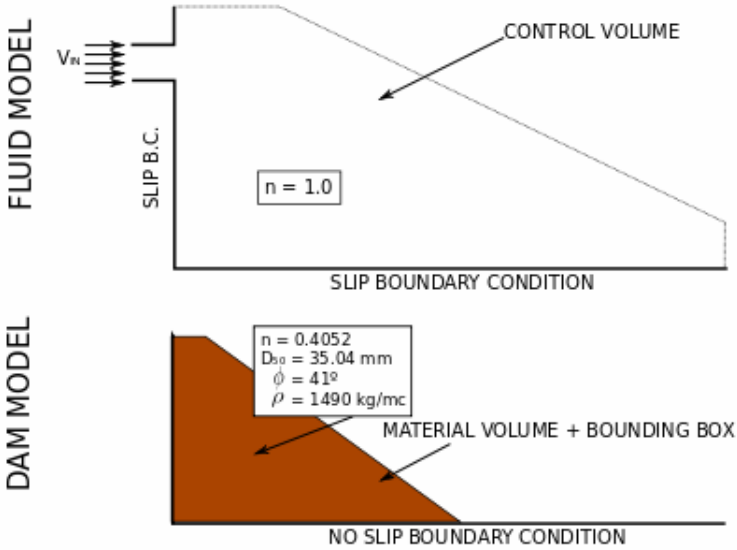


Figure 19. Cases B2. Fluid and dam qualitative models and boundary conditions for the coupled analysis.

It is observed an excessive deformation in the case of 40° friction angle tangent, therefore $\phi = 41^\circ$ is the chosen angle. This difference is not so relevant according to the uncertainties (of the order of some degrees) that experimentalists have in defining this value.

Figure 20 shows the mesh used in the structural model. It is composed of 8000 linear triangular elements.

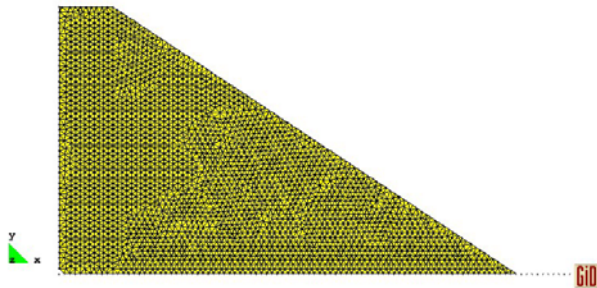


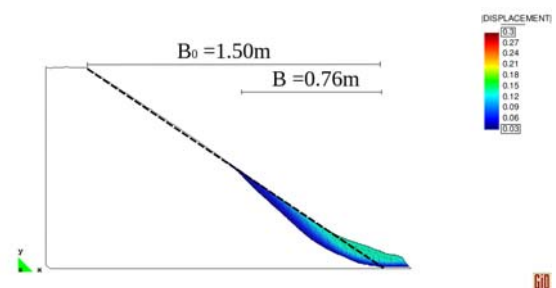
Figure 20. Cases B2. 2d mesh of the dam model. 8.000 linear triangular elements.

2.4.1. Case B21: $Q=19.36/s$

Looking at Figure 21 it can be observed that the numerical prediction of failure is much larger than in the experiment ($B_{exp} = 0.32m$ whereas $B_{num}=0.76m$) but the amount of moved volume is lower in the simulated one. In fact the experimental pressure at the toe of the dam (Figure 22) is lower than the numerical. This, as already pointed out for case A23 can be the consequence of the visco-rigid model chosen. When shear stresses decrease under yield stress limit viscosity dramatically increases causing a sudden stop of the flowing of the failed material.



a) Experimental length of failure $B_{exp} = 0.32m$



b) Numerical length of failure $B = B_{num} = 0.76 m$

Figure 21. Case B21. 2d comparison between experimental and numerical length of failure.

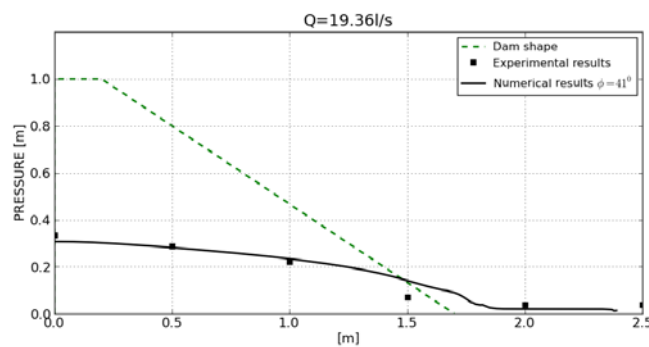


Figure 22. Case B21. 2d comparison between experimental and numerical pressure heads at stationary regime.

In order to investigate the cause of this overestimation a series of friction angles from 40° to 42° degrees have been taken into account showing that the minimum angle for which the dam deforms is 41.5° and the deformation is analogous to the one observed in Figure 21(b).

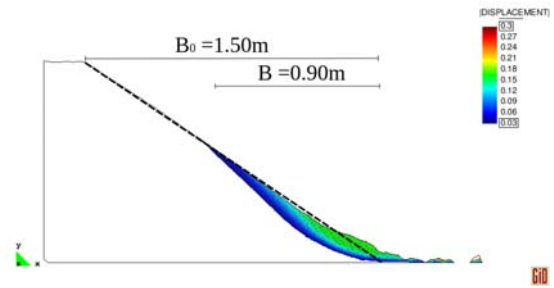
The model seems unable to catch deformations that are much smaller than the half of the horizontal projection of the down stream slope (B_0). This observation is confirmed in case C21 (see section 2.6.1) whereas it is not appreciated in case A21 because the length of failure is almost the half of B_0 (see Figure 11).

2.4.2. Case B22: $Q=30.45/s$

The numerical length of failure shown in Figure 23 is higher than the experimental value although the pressure distribution (Figure 24) presents a good accordance indicating the correct calculation of the hydrodynamic forces.



a) Experimental length of failure $B_{exp} = 0.68\text{m}$



b) Numerical length of failure $B = B_{num} = 0.90\text{m}$

Figure 23. Case B22. 2d comparison between experimental and numerical length of failure.

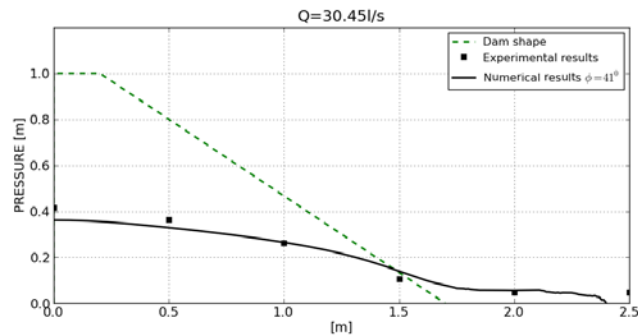


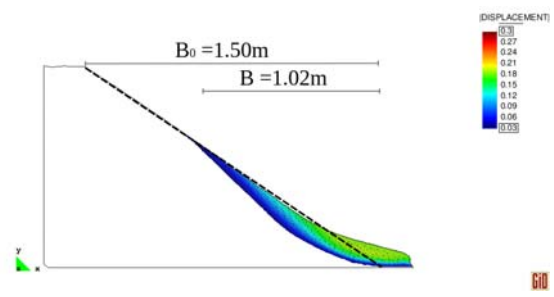
Figure 24. Case B22. 2d comparison between experimental and numerical pressure heads at stationary regime.

2.4.3. Case B23: $Q=39.56\text{l/s}$

A short remark should be made here on the experimental length of failure taken as reference. Theme B reports $B_{exp} = 1.40\text{m}$ but taking a look at Figure 25(a) it is evident that a 2d model cannot reproduce the 3 dimensional consequences of erosion. In fact the latter induces the formation of this “channel” in the center of the dam. That is the reason why, from a visual measurement B_{exp} is taken equal to 1.00m , which is the level at which the failure induced by mass sliding arrived (just under the blue line of Figure 25(a)).



a) Experimental length of failure $B = B_{exp} = 1.00\text{m}$



b) Numerical length of failure $B = B_{num} = 1.02\text{m}$

Figure 25. Case B23. 2d comparison between experimental and numerical length of failure.

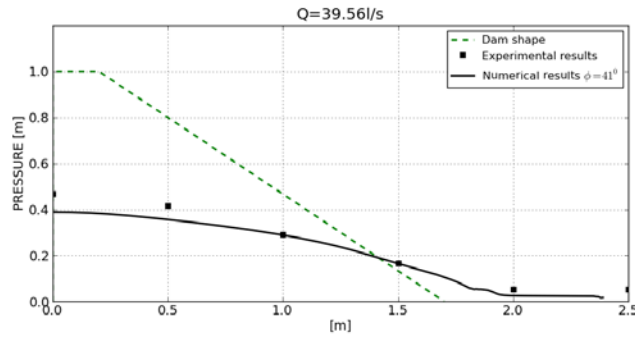


Figure 26. Case B23. 2d comparison between experimental and numerical pressure heads at stationary regime.

Therefore, taking into account the previous consideration, the accordance of experimental and numerical results shown in Figure 25 and Figure 26 is good.

2.5. Case C1

The simulation of a dam with and impervious screen is the most challenging case from a fluid dynamic point of view. The inlet of water is set in the upper left part, according to what already done in case B therefore a falling jet should be simulated. This is the reason why the mesh (see Figure 27) is finer in the area where the jet falls and impact with the bottom.

The accordance of experimental and numerical pressure heads is good (see Figure 28) except for some very interiors points that experimentally presents some oscillations maybe induced by local phenomena caused by the presence of the impervious screen.

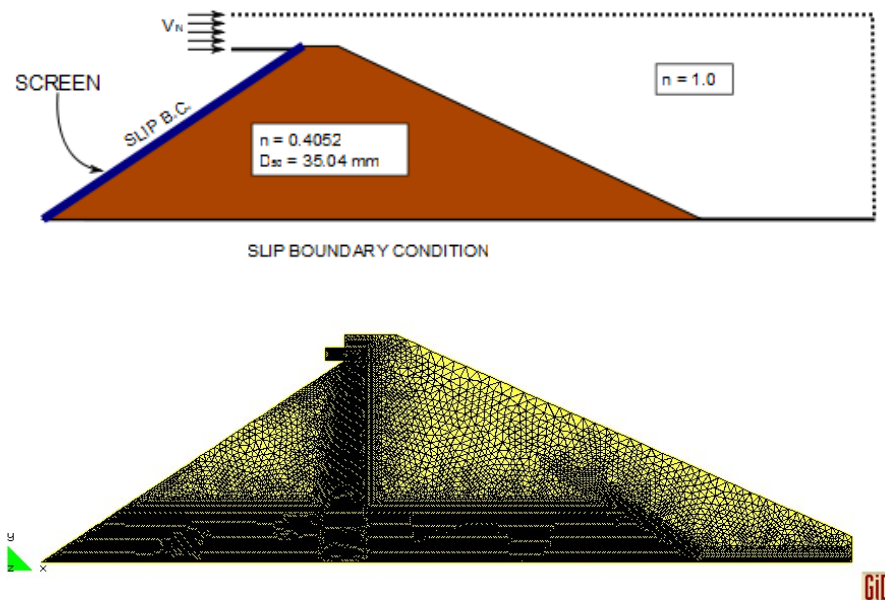


Figure 27. Case C1. Qualitative model geometry and boundary conditions in the upper image and calculation mesh in the lower one.

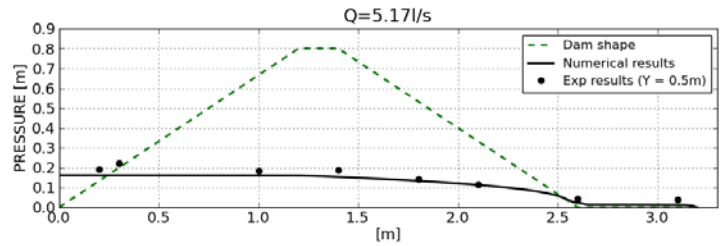


Figure 28. Case C1. 2d comparison between experimental and numerical pressure heads at stationary regime.

2.6. Case C2

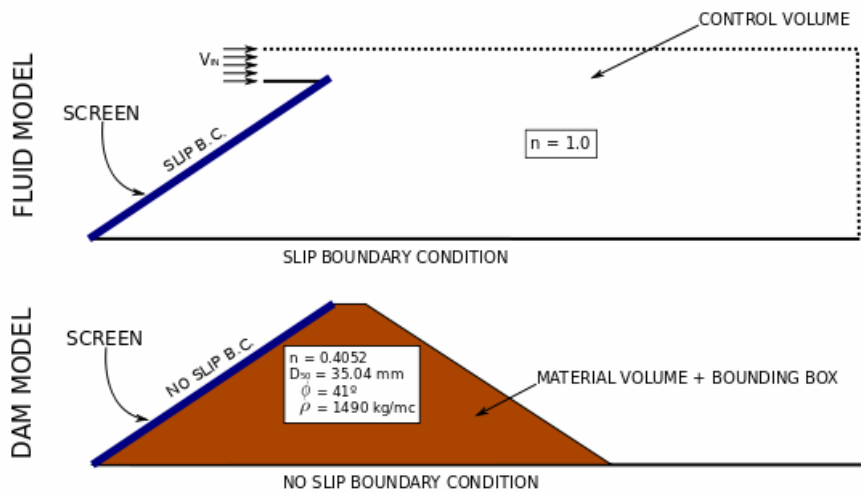


Figure 29. Cases C2. Fluid and dam qualitative models and boundary conditions for the coupled analysis.

The construction of the models for the coupled analysis is done according to what already explained for case A2 and B2 and it is shown in Figure 29.

The mesh used in the fluid model is exactly the same than in the C1 case (see Figure 27) whereas the mesh of the dam is shown in Figure 30.

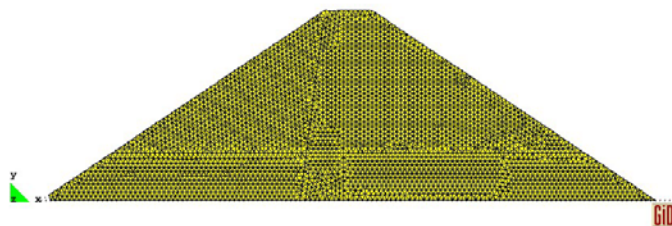


Figure 30. Cases C2. 2d mesh of the dam model. 9.400 linear triangular elements.

2.6.1. Case C21: $Q=15.36l/s$

Looking at Figure 31 it can be observed that the coupled model overestimates the length of failure in case C1. Its performance will improve with higher discharges, as will be explained in the following sections.

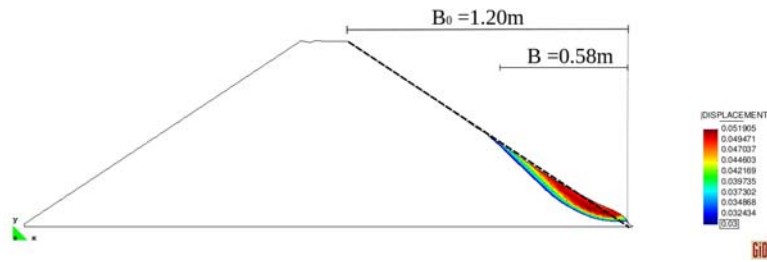


Figure 31. Case C21. 2d comparison between experimental ($B_{exp} = 0.24\text{m}$) and numerical length of failure ($B_{num} = 0.58\text{m}$).

The overestimation of the length of failure when $B_{exp} \ll B_0$ has already been commented in section 2.4.1.

The pressure head distribution (see Figure 32) presents a good matching although the excessive movement of the material can be the cause of the higher numerical pressure out of the toe of the dam.

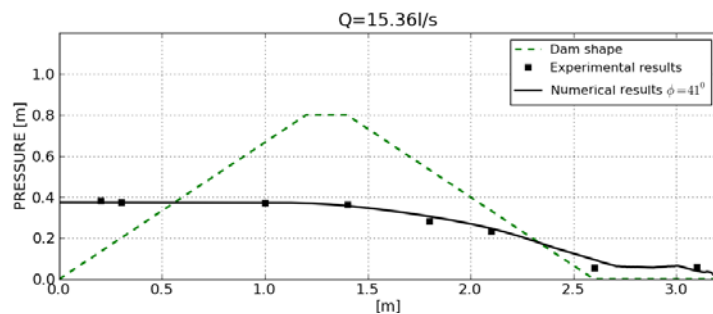


Figure 32. Case C21. 2d comparison between experimental and numerical pressure heads at stationary regime.

2.6.2. Case C22: $Q=25.05\text{l/s}$

In case C22 the numerical length of failure is $B_{num} = 0.61$, as shown in Figure 33, which is close to the experimental value $B_{exp} = 0.59\text{m}$. Nevertheless the numerical pressure heads are lower than the experimental one (Figure 34).

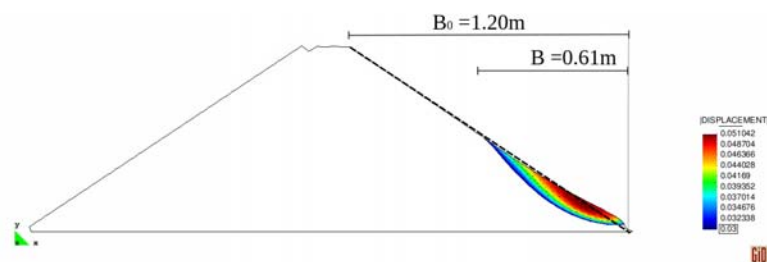


Figure 33. Case C22. 2d comparison between experimental ($B_{exp} = 0.59\text{m}$) and numerical length of failure ($B_{num} = 0.61\text{m}$).

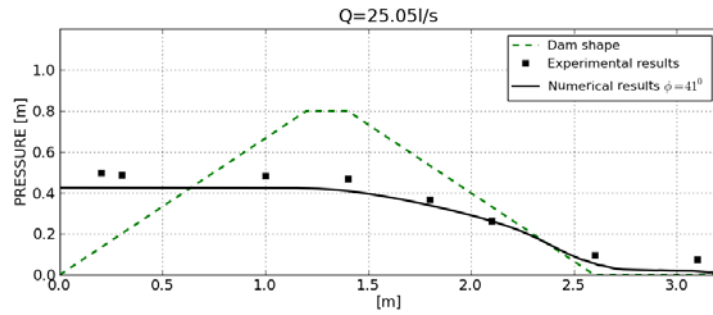


Figure 34. Case C22. 2d comparison between experimental and numerical pressure heads at stationary regime.

2.6.3. Case C23: $Q=30.27l/s$

In the last example the failure achieves the crest of the dam both in the numerical ($B_{num} = 1.40m$) and in the experimental ($B_{exp} = 1.44m$) models (see Figure 35).

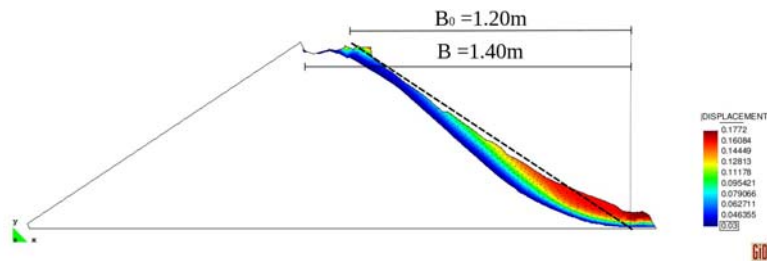


Figure 35. Case C23. 2d comparison between experimental ($B_{exp} = 1.44m$) and numerical length of failure ($B_{num} = 1.40m$).

A good accordance can be found in the pressure head distribution, as shown in Figure 36

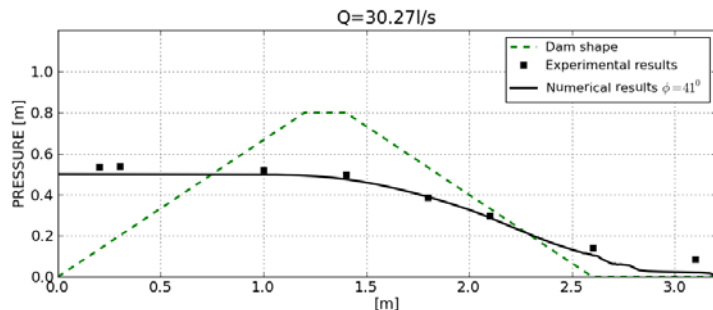


Figure 36. Case C23. 2d comparison between experimental and numerical pressure heads at stationary regime.

4. Conclusions

In the present work an innovative approach for the simulation of failure of rockfill slope is presented.

The dynamic evolution of seepage and the free surface flow both upstream and downstream the dam are analyzed at once using a modified form of the Navier-Stokes equations where the effect of seepage is considered using a quadratic form of the Darcy law.

The structural response is evaluated with a visco-rigid constitutive model and using a Mohr Coulomb failure criteria. The rockfill material is considered a high viscosity non-Newtonian fluid. The viscosity drastically decreases when, due to the hydrodynamic effect, the yield stress is exceeded causing the formation of a failure circle and the subsequent flowing of the material.

The coupling is performed using a fully staggered scheme and a projection tool between non-matching meshes.

Concerning the simulation of the experiments proposed in theme B, the conclusions are:

1. The fluid module:

- There is a good accordance between experimental and numerical pressure heads in the undeformed cases (A1, B1, C1) both in 2 and 3d.
- This is not always reflected in the partially failed experiments. In the interior of the dam this can be the consequence of local consolidation of the material that is not taken into account in the models. On the other hand, at the toe of the dam, this can be the consequence of a smaller deformation of the failed material. Whereas the length of failure is correctly reproduced, the failed material settles faster than in the real case.
- The code presents a good performance also in the challenging cases of a falling jet of water.
- Another challenging aspect of the undeformed cases is that the discharges are very low. This could represent a problem at the beginning of the simulation when a very thin layer of water starts filling the dam. This problem can be easily overcome refining the mesh close to the bottom.

2. The coupled module:

- In the paper it was pointed out the low reliability of B parameter used to quantify the length of failure.
- The code represents the incremental failure of the dam when increasing the overspilling discharge.
- It is able to represent correctly the cases in which failure achieves the crest of the dam. On the contrary with lower discharges it is overestimated.
- As already observed in the conclusions regarding the fluid module, the failed material settle faster than in the real case. This can be a consequence of the chosen visco-rigid constitutive model. In fact when the shear stress decreases under the yield stress threshold the viscosity dramatically increases causing a sudden stop of the element.

3. Additional conclusions:

- The code was conceived to analyze the transitory phase of the discharge, allowing inserting flood hydrograms as input although in these examples this capability is not exploited.
- It would be interesting the comparison of the failure surfaces.

Acknowledgements

The research was supported by the E-DAM project of the National Plan R+D of the Spanish Ministry of Science and Innovation I+D BIA2010-21350-C03-00.

References

- [1] E-DAMS Numerical and experimental techniques for safety assessment and protection of embankment dams in overtopping scenarios project of the National Plan R+D of the Spanish Ministry of Science and Innovation I+D BIA2010-21350-C03-00, 2010-2013
- [2] Dadvand, P. & Rossi, R. & Oñate, E. (2010) An object-oriented environment for developing finite element codes for multi-disciplinary applications Archives of Computational Methods in Engineering, 17, 253-297
- [3] Idelsohn, S.R., Oñate, E. and Del Pin, F., 2004, The Particle Finite Element Method: a powerful tool to solve incompressible flows with free-surfaces and breaking waves, International Journal for Numerical Methods in Engineering, 61, 964-984.
- [4] Kratos multiphysics opensource fem code, <http://www.cimne.com/kratos>
- [5] Larese, A. & Rossi, R. & Oñate, E. & Idelsohn, S.R. (2008), Validation of the particle finite element method (PFEM) for simulation of free surface flows, Engineering Computations , 25, 385-425.
- [6] Larese, A. (2011) Development of a numerical algorithm to simulate free surface problems in a variable porosity medium. An application to the analysis of flow through rockfill dams. . Master Thesis. Master en métodos Numéricos para Cálculo y diseño en Ingeniería.
- [7] Oñate, E. & Celigueta, M.A. & Idelsohn, S.R. (2006) Modeling bed erosion in free surface flows by the particle finite element. Acta Geotechnica, Vol 1, pp 237-252.
- [8] Oñate, E., Idelsohn, S.R., Celigueta, M.A., Rossi, R., 2008, Advances in the particle finite element method for the analysis of fluid-multibody interaction and bed erosion in free surface flows, Computational methods in Applied Mechanics and Engineering, Vol. 197, 1777-1800.
- [9] Papanastasiou, T. C. (1987). Flows of materials with yield. Journal of Rheology 31, 385-404.
- [10] The particle finite element method PFEM <http://www.cimne.com/pfem/>
- [11] Ryzhakov, P. & Rossi, R. & Oñate, E. An algorithm for the simulation of thermally coupled low speed flow problems Int. Journal for Num. Methods in Fluids, 2011
- [12] Rossi, R. & Larese, A. & Dadvand, P. & Oñate, E. (2011) An efficient edge-based level set finite element method for free surface flow problems Submitted to: International Journal for Computational Methods in Fluids.
- [13] XPRES “Desarrollo de un método para el estudio del proceso de rotura de presas de escollera por sobreevertido combinando técnicas de elementos finitos y partículas”, XPRES project of the National Plan R+D of the Spanish Ministry of Science and Innovation I+D BIA2007-68120-C03-01
- [14] Zienkiewicz, O.C. & Chan, A.H.C. & Pastor, M. & Schrefler & B.A., Shiomi, T. (1998) Computational geomechanics, with special reference to earthquake engineering, Ed. Wiley.
- [15] Zienkiewicz, O. & R. Taylor, & P. Nitharasu (2005). Vol. 3. The finite element method. Fluid dynamics. Elsevier.